PNAS | RESEARCH ARTICLE | IMMUNOLOGY AND INFLAMMATION | OPEN ACCESS

Lethal COVID-19 associates with RAAS-induced inflammation for multiple organ damage including mediastinal lymph nodes

Michael J. Topper[a,b,1], Joseph W. Guarnieri[a,c,d,1], Jeffrey A. Haltom[a,c,d], Amy Chadburn[e], Henry Cope[f], Justin Frere[g], Julia An[a,b], Alain Borczuk[h], Saloni Sinha[h], JangKeun Kim[h], Jiwoon Park[h], Daniel Butler[h], Cem Meydan[h], Jonathan Foox[h], Yaron Bram[h], Stephanie A. Richard[i,j], Nusrat J. Epsi[i,j], Brian Agan[i,j], Josh G. Chenoweth[j], Mark P. Simons[i], David Tribble[i], Timothy Burgess[i], Clifton Dalgard[k], Mark T. Heise[l], Nathaniel J. Moorman[l], Victoria K. Baxter[l], Emily A. Madden[l], Sharon A. Taft-Benz[l], Elizabeth J. Anderson[l], Wes A. Sanders[l], Rebekah J. Dickmander[l], Katherine Beigel[a,c,m], Gabrielle A. Widjaja[a,c,d], Kevin A. Janssen[a,c,d], Timothy Lie[a,c,d], Deborah G. Murdock[a,c,d], Alessia Angelin[a,c,d], Yentli E. Soto Albrecht[a,c,d,n], Arnold Z. Olali[a,c,d], Zimu Cen[a,c,d], Joseph Dybas[a,c], Waldemar Priebe[a,o], Mark R. Emmett[a,p], Sonja M. Best[a,q], Maya Kelsey Johnson[a,b], Nidia S. Trovao[a,r], Kevin B. Clark[a,s,t], Victoria Zaksas[a,u,v], Robert Meller[a,w], Peter Grabham[a,x], Jonathan C. Schisler[a,l], Pedro M. Moraes-Vieira[a,y], Simon Pollett[i,j], Christopher E. Mason[a,h,z], Eve Syrkin Wurtele[a,aa,bb,cc], Deanne Taylor[a,c,d,m,dd], Robert E. Schwartz[a,h], Afshin Beheshti[a,ee,ff,gg,1,2], Douglas C. Wallace[a,c,d,hh,1,2], and Stephen B. Baylin[a,b,ii,1,2]

Affiliations are included on p. 11.

Contributed by Stephen B. Baylin; received February 15, 2024; accepted October 7, 2024; reviewed by Preetam Ghosh and Ira Mellman

Lethal COVID-19 outcomes are attributed to classic cytokine storm. We revisit this using RNA sequencing of nasopharyngeal and 40 autopsy samples from patients dying of SARS-CoV-2. Subsets of the 100 top-upregulated genes in nasal swabs are upregulated in the heart, lung, kidney, and liver, but not mediastinal lymph nodes. Twenty-two of these are "noncanonical" immune genes, which we link to components of the renin-angiotensin-activation-system that manifest as increased fibrin deposition, leaky vessels, thrombotic tendency, PANoptosis, and mitochondrial dysfunction. Immunohistochemistry of mediastinal lymph nodes reveals altered architecture, excess collagen deposition, and pathogenic fibroblast infiltration. Many of the above findings are paralleled in animal models of SARS-CoV-2 infection and human peripheral blood mononuclear and whole blood samples from individuals with early and later SARS-CoV-2 variants. We then redefine cytokine storm in lethal COVID-19 as driven by upstream immune gene and mitochondrial signaling producing downstream RAAS (renin-angiotensin-aldosterone system) overactivation and organ damage, including compromised mediastinal lymph node function.

COVID-19 | fibrosis | renin angiotensin aldosterone system

COVID-19, caused by the single-stranded RNA virus, severe acute respiratory syndrome coronavirus 2 (SARS-CoV-2), is responsible for extensive global morbidity and mortality (1). Various studies have probed the molecular underpinnings of patient responses to the virus for the most severe consequences. These studies employed RNA sequencing (RNAseq) analyses of nasal swabs and blood cells but less often visceral tissues (2, 3). Initial RNAseq analysis of nasal swabs and cell models showed that a deficit in responses of classic interferon (IFN) driven viral defense genes might account for overactive innate immune responses in infected patients. However, subsequent analyses indicated IFN genes are robustly upregulated, especially in the nasopharynx (2, 4). RNAseq and metabolomic analysis of bronchoalveolar lavage fluid (BALF), whole blood, and serum collected from severe COVID-19 patients displayed excessive cytokine levels correlating with COVID-19 severity (3, 5, 6). However, no studies have investigated the effect of COVID-19 on the immune system in a full spectrum of autopsy organs, which is imperative to understanding how deficits in innate and adaptive immune responses can result in tissue damage leading to lethal outcomes (7).

Many critically ill patients with COVID-19 and post-acute sequelae of COVID-19 (PASC) have shown damage to multiple organ systems, including severe lung, kidney, and cardiac injury, liver dysfuction (8), and lymphedema (9). One possible explanation for this widespread organ damage might be a chronic overactivation of RAAS (10, 11). RAAS normally regulates blood pressure but, when chronically overactivated, triggers a cascade of inflammatory tissue-damaging events, which are prominent in hereditary angioedema (HAE), an organ dysfunction disorder with similarity to severe COVID-19 (10). Proper regulation of RAAS activity is controlled by ACE2, the receptor for cellular entry of SARS-CoV-2, and a key upstream event for RAAS overactivation is the reduction of ACE2 (10). Indeed, one BALF RNAseq study of severe COVID-19 patients reported altered levels of two RAAS components, bradykinin and hyaluronic acid (HA), and decreased levels of SERPING1, which normally inhibits RAAS signaling to balance complement activity levels. Our data suggest that severe COVID-19 reflects a disease driven by a "bradykinin storm", wherein a vascular leak syndrome results in severe pulmonary inflammation with respiratory compromise and risk of thrombosis (12).

Previous studies have reported mitochondrial dysfunction in COVID-19, revealing that mitochondrial defects activate the innate immune system by disrupting mitochondrial oxidative phosphorylation (OXPHOS) and elevating mitochondrial reactive oxygen species (mROS) (7). The result is a release of mitochondrial DNA (mtDNA) and mitochondrial double-stranded RNA (mtdsRNA) into the cytosol (13, 14). Cytosolic mtDNA and mtdsRNA can be detected by innate

Significance

This work defines across multiple large, independent patient cohorts the downstream implications of cytokine storm in lethal COVID-19 as driven by upstream immune gene and mitochondrial signaling producing RAAS overactivation and subsequent organ damage. Furthermore, we delineate a lymphoid organ fibrosis phenotype occurring in severe COVID-19, which has potential implications in mediating the chronic B and T cell dysfunction prevalent in long COVID. Correlations between tissue findings and circulating markers suggest this last possibility.

Reviewers: P.G., Virginia Commonwealth University; and I.M., Genentech, Inc.

Competing interest statement: R.E.S. is on the scientific advisory of Miromatrix, Inc. and Lime Therapeutics and is a consultant for Alnylam, Inc. D.C.W. is on the scientific advisory boards of Pano Therapeutics, Inc., and Medical Excellent Capital.

[1] M.J.T., J.W.G., A. Beheshti, D.C.W., and S.B.B. contributed equally to this work.

[2] To whom correspondence may be addressed. Email: beheshti@pitt.edu, walladced1@chop.edu, or sbaylin@jhmi.edu.

This article contains supporting information online at https://www.pnas.org/lookup/suppl/doi:10.1073/pnas.2401968121/-/DCSupplemental.

immune sensors, resulting in the activation of an innate immune response and initiation of cell death pathways (6, 13–17). Hence, viral inhibition of mitochondrial bioenergetics may play an essential role in the activation and intensity of SARS-CoV-2-induced inflammation.

We now rigorously probe how damage to multiple organs may occur in patients with lethal outcomes from COVID-19 by comparing transcriptomic changes in nasopharyngeal samples and autopsy tissues and performing histopathology measurements to validate immune defects correlated with RAAS activation as suggested by our transcriptomic findings. We link transcriptional changes to the critical role of mitochondrial damage, which induces this organelle to act as a gateway to activation of the innate immune response and integrated stress response (ISR). Further, we validate our findings in murine models of SARS-CoV-2 infection and through examination of peripheral blood mononuclear cells (PBMCs) and whole blood samples from individuals infected with both early and later SARS-CoV-2 variants.

A significant finding is that in nasopharyngeal samples, the top-upregulated innate and adaptive immune genes are linked as upstream signals to extensive gene alterations corresponding to RAAS-overactivation. Our results reveal a complex interplay between upstream immune gene signaling and downstream RAAS activation to induce lethal damage to multiple organ systems and an expanded view of the cytokine storm concept in COVID-19 (18). While others have suggested this RAAS paradigm (11), detailed primary data for the full spectrum of events have been lacking in the COVID-19 literature. Our present work now indicates the involvement of many genes not previously focused upon, highlighting components of overactive RAAS signaling, such as PANoptosis, a process mediating multiple modes of cell death. A seminal finding, which we document with laboratory studies, is how the RAAS component of excess fibrin deposition and associated collagen deposition is associated with fibroblast infiltration of the mediastinal lymph nodes, correlating with altered lymph node architecture, histological indicators of fibrosis, and immune cell abnormalities, which may all contribute to a reduced immune response integral to COVID-19 patient mortality.

Results

Sample Collection for RNAseq Analysis and SARS-CoV-2 Viral Load. We quantified the relative expression level of human and SARS-CoV-2 transcripts from RNAseq data collected from 735 nasopharyngeal and in 40 lung, heart, kidney, liver, and mediastinal lymph node autopsy samples SARS-CoV-2 positive and negative individuals. Our analysis revealed high levels of SARS-CoV-2 transcripts in the human nasopharyngeal samples, but virtually undetectable SARS-CoV-2 transcripts in the human autopsy samples (*SI Appendix*, Table S1).

As we could not correlate analyses with precise time points after COVID-19 diagnosis, we analyzed expression levels of host genes and SARS-CoV-2 genes in RNAseq data from SARS-CoV-2 infected Syrian hamsters and C57BL/6 and BALB/c mouse models, where sample collection timing is controlled. Samples were collected when viral titers had peaked in the lung. In the mice, lung samples were also collected after peak viral titers (*SI Appendix*, Table S1). SARS-CoV-2 gene transcripts were highest in the hamster lungs, followed by the BALB/c and C57BL/6 mouse lungs, while no significant levels of SARS-CoV-2 transcripts were detected in the hamster heart, kidney, or brain (striatum, cerebellum, olfactory bulb). Together, these analyses enabled us to assess COVID-19 progression early in infection in the nasopharyngeal and hamster samples, mid-infection in the mice, and after the virus had been cleared in the human autopsy tissues.

Early-Stage Transcript Changes in Human Nasopharyngeal Samples.

Individual responses to SARS-CoV-2 infection. To survey individual gene expression responses to SARS-CoV-2, a z-score vector of gene expression for positive samples versus PCR "None" group was generated per nasopharyngeal sample, and the ranked z-score vector was used for gene enrichment analysis versus selected gene sets (*SI Appendix*, Table S2). Fig. 1*A* shows the normalized enrichment score (NES) results within the Hallmark IFNα gene set and reveals that for most immune-related gene sets, the group effects were significantly linear for the amount of PCR-detected SARS-CoV-2 between groups.

Upregulated, canonical innate immune genes. We next determined relative gene expression levels from RNAseq data in SARS-CoV-2 positive and negative nasopharyngeal samples (Fig. 1 *B–E*) fitted for viral load using curated gene lists to characterize the highest up- and down-regulated genes in samples from COVID-19 infected versus negative patients to guide subsequent analyses.

Twenty-nine of the most differentially upregulated genes, which we term "canonical" innate immune genes, are the well-known IFN-driven and sensitive (ISG) genes for proteins processing viral dsRNA, including *IFIH1, IFIT2, OAS1-3, STAT2, ISG20, DDX60*, and *ISG15* among others (Fig. 1 *B–D*). These canonical genes again stratify with increasing viral load (Fig. 1*D*) and with induction of the IFNα gene set enrichment analysis (GSEA) pathway (Fig. 1*A*). All canonical genes were upregulated except for *IL1A,* which was down-regulated (Fig. 1*D*). Importantly, IL1A is released from infected cells to signal immune clearance (19); thus, its downregulation could prevent these cells from being cleared. Additionally, several genes for protein assembly factors for surface expression of the histocompatibility complex (MHC) 1 allow complex antigen recognition and NF-κB and TNF-related genes were upregulated.

Noncanonical innate immune genes. Among the most differentially upregulated genes are 22 ISGs, not generally noted in COVID-19 papers but designated in literature as IFN, ISG genes. We termed these "noncanonical" innate immune genes (Fig. 1 *B–D*). These genes were stratified with increasing viral load in nasal swab samples and were all significantly upregulated except for *CMTM4*, whose downregulation may contribute to a heightened inflammatory state through reduced membrane retention of PD-L1 (20). Importantly, these genes encode proteins that play important roles throughout our narrative, and some key aspects include: 1) SERPING1, crucial for controlling complement pathway activation, a key event in severe tissue-damaging inflammation (10, 21); 2) PLVAP, an endothelial cell-specific membrane protein required for controlling microvascular permeability and barrier function of gut endothelium (22); when deleted in mice triggers fluid and protein leakage into surrounding tissues and premature death (23). 3) RNF213, a C3HC4-type RING-finger domain that facilitates Class I MHC antigen processing and presentation and Wnt-signaling inhibition (24, 25). 4) HERC5/6, both of which act as antiviral IFN proteins interacting with ISG15, an ISGylation ligase-type enzyme that targets viral-RNA/proteins for degradation (26–28). 5) Five poly (ADP-Ribose) polymerase (PARP) genes are upregulated (Fig. 1*D*), which respond to cellular stressors, including oxidative stress, DNA damage, and pathogen infection (29). Most PARPs are ribosylases and MARylases, blocking the translation of viral RNAs and targeting viral proteins for degradation (29). Notably, several upregulated noncanonical genes, encoding ZNFX1, ZBP1, GSDMB, XAF1, and CMPK2, utilize mitochondria to facilitate activation of the innate immune system. Among these, the top one, *ZNFX1,* encodes a zinc finger helicase, which, upon viral infection, recognizes viral dsRNA and shuttles to the outer mitochondrial membrane to restrict viral replication (30, 31). ZBP1 has the potential to induce multiple modes of cell death, including apoptosis, pyroptosis, necroptosis, and PANoptosis (32–35) (Fig. 1*D*). GSDMB is an integral member of the gasdermin (GDSM) family of death mediators (36); XAF1 mediates TNFα-induced apoptosis (37); CMPK2 stimulates mtDNA synthesis, a key dynamic for inducing inflammasome signaling (13, 38).

Down-regulated IL-1 family and antimicrobial response-associated genes. Eighty-three genes displayed a significant negative association with viral load in the nasopharyngeal samples (Fig. 1 *B* and *E*). These genes encompass seven functional categories including 1) four sulfonation-associated genes (*SULT2B1, SULT1E1, SULT1B1, PAPSS2*); 2) seven selenoamino acid metabolism (*RPL4/5/6/7, RPS3A/4X/S6*) genes; 3) twenty-five cornification and keratinization-associated genes; 4) eight antimicrobial peptide/degranulation genes; and 5) eight IL-1 family genes. The latter two categories have been previously suggested to be cytokine storm components during SARS-CoV-2 infection (39), and sulfonation and selenoamino acid metabolism gene upregulation indicate the potential involvement of keratinocytes in SARS-CoV-2 nasopharyngeal pathogenesis.

Later-Stage Transcript Changes in Human Autopsy Tissues and Rodent Antecedents. To better understand inflammation processes that underlie severe COVID-19, we compared transcription in the nasopharyngeal samples to a multitude of autopsy tissues and further validated key findings in SARS-CoV-2 infected-hamster and -C57BL/6 and -BALB/c mice.

Comparison of canonical, inflammation, and antigen presentation genes. Despite the absence of SARS-CoV-2 transcripts, activation of immune and inflammatory genes is seen in all assessed tissues

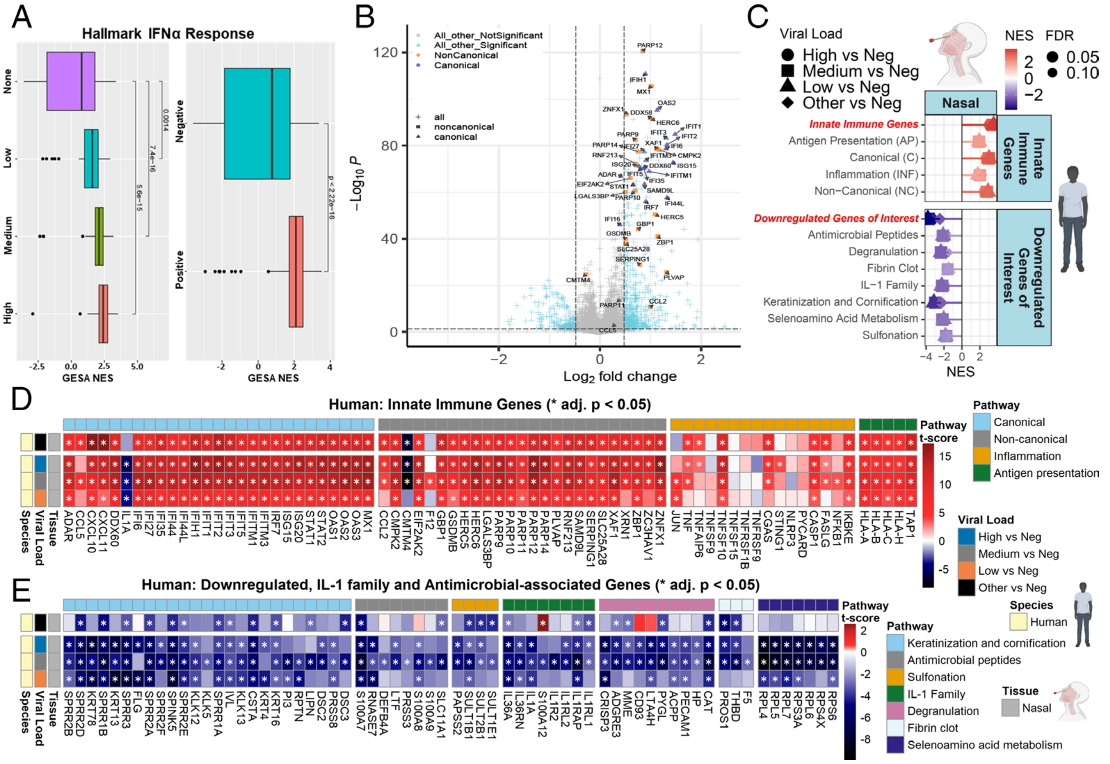

Fig. 1. Early-stage innate immune gene expression in nasopharyngeal samples from COVID-19 patients. (*A*) Box and whisker plot of hallmark interferon alpha response gene sets determined by fGSEA for nasopharyngeal samples ranked by NES (nominal enrichment score). (*B*) Volcano plots of nasopharyngeal samples with high, SARS-CoV-2 RNA copy levels at collection. (*C*) Lollipop plots for custom gene sets determined by fGSEA (FDR < 0.25), ranked by NES. (*D* and *E*) Heatmaps of *t* score statistics when comparing viral load versus negative patient samples for specific (*D*) innate immune genes and (*E*) downregulated genes of interest, IL-1 family and antimicrobial-associated genes.

except for liver and lymph nodes. In total, 25 canonical immune genes highly expressed in nasopharyngeal samples retain significant upregulation across the heart (17 genes), kidney (17 genes), and lung (14 genes) (Fig. 2). In sharp contrast, in both liver and lymph nodes, only 2 genes are upregulated, and 7 are down-regulated, including those encoding Type 1 (HLA) associated genes (Fig. 2*A*). In lung, heart, and kidney as compared to a lesser extent in the nasopharyngeal samples, there is robust upregulation of death-associated TNF-superfamily (TNFSFs) genes that accompany IFN-signaling (40) (Fig. 2*A*) including *TNSF10* in heart, and *TNSF1/5/9* and *TNFAIP6* in the lung. Additionally, *CXCL10/11* are upregulated in lung, heart, kidney, and nasopharyngeal samples (Fig. 2*A*). CXCL10 is a potent inflammatory cell chemotactic chemokine known to be increased in the serum of severe COVID-19 patients (41) and mouse lungs infected with SARS-CoV-2 (42).

Noncanonical genes in autopsy tissues. The genes, introduced in the preceding section and all highly expressed in nasopharyngeal swab samples, present a more heterogenous expression in autopsy tissue samples (Fig. 2*A*). These include: 1) *GBP1, IFNγ,* and cytokine signaling genes (43), retaining high expression levels in the lung, heart, and kidney (Fig. 2*A*); 2) *HERC5/6* associate with canonical immune gene *ISG15* the former of which retains high expression in lung, heart, and kidney (Fig. 2*A*); 3) the ISR initiating genes *EIF2AK2* and *MX1* (44) are upregulated in the nasopharyngeal samples, but this augmentation is only retained in the kidney with significant downregulation noted the in mediastinal lymph nodes. *PARP9/12/14,* highly upregulated in the nasopharyngeal samples, remained upregulated in the autopsy lung, heart, and kidney (Fig. 2*A*). Additionally, *ZBP1, GSDMB, XAF1,* and *CMPK2* upregulated in the nasopharyngeal samples, retain their high expression in the lung, heart, and kidney and, to a lesser extent, in the liver.

Particular implications of innate immune gene expression in mediastinal lymph nodes. Only 5 of 36 robustly upregulated innate immune genes in nasopharyngeal samples retain upregulation in mediastinal lymph nodes, while 15 are down-regulated. Upregulated canonical IFN genes are *IFITM3, ISG15,* and *STAT2;* noncanonical genes are *RNF213* (45) and DNA damage sensing genes *CGAS* and *STING1.* The 15 reduced genes include 5 MHC1-related genes and also *ZNFX1, SERPING1,* and *PVLAP,* for which reduced expression can contribute to cell death/inflammation (21, 22, 46), and *HERC5/6,* which upregulates *ISG15* (27) (Fig. 2*A*). The critical implications of these expression patterns for compromised mediastinal lymph node immune function is addressed in more detail later.

Downregulated genes of interest in the autopsy tissues. Expanding our assessment of downregulated genes identified in the nasopharyngeal samples to human autopsy and animal model tissues revealed that these gene patterns were primarily relegated to nasopharyngeal samples (*SI Appendix*, Fig. S1) with several notable exceptions. Antimicrobial peptide/degranulation genes were downregulated in the lymph nodes and across both human and mouse lung samples, and IL-1 family genes were downregulated in the hamster lung and heart samples (*SI Appendix*, Fig. S1*B*). In total, our data showed that SARS-CoV-2 viral load has a negative association with genes in the broad classes of the IL-1 family, sulfonation/selenoamino acid metabolism, antimicrobial, and cornification/keratinization. The association of viral load and tissue site with IL-1 and degranulation highlights the importance of tissue-level specificity when assessing host responses to viral infection.

Gene expression in SARS-CoV-2 infected rodents. Like our human tissues, the lung, heart, and kidney of hamsters and lung of C57BL/6 and BALB/c mice show significant upregulation of most canonical and noncanonical innate immune genes. In the hamster brain, innate immune gene pathways were upregulated in the olfactory bulb and, to a lesser extent, in the cerebellum and striatum (Fig. 2 *A* and *B* and *SI Appendix*, Figs. S2 and S3). Treatment of C57BL/6 and BALB/c mice with baricitinib or tofacitinib, which act as Janus kinase inhibitors, decreased activation of innate immune gene pathways (*SI Appendix*, Figs. S4 and S5). Together, these results demonstrate that innate immune genes are upregulated in the presence of replicating virus in early- and mid-infection in the human nasopharyngeal and rodent tissues and maintained despite the evidence of viral infection in other tissues.

Germline mutations in innate immune genes produce symptoms widely overlapping with those in severe COVID-19 patients. Considering syndromes induced by germline mutations in canonical and noncanonical genes (*SI Appendix*, Fig. S6 and Table S3) provides critical clues to the importance of their dysregulation for lethal, inflammatory consequences in COVID-19. Such mutations of canonical immune genes produce Aicardi–Goutières syndromes (AGS) wherein overexpression of IFN-signaling genes results in constitutive cytokine-storm and often lethal outcomes in children (47) (*SI Appendix*, Fig. S6 and Table S3). In rare families, loss-of-function germline mutations in *ZNFX1,* our top upregulated noncanonical gene in nasopharyngeal samples, produce often-lethal overaction of IFN-signaling only when affected individuals encounter pathogens (30). *ZNFX1* is highly expressed in nasal swab samples but has little to no expression in all autopsy samples (Fig. 2*A* and *SI Appendix*, Fig. S6 and Table S3). As outlined in *SI Appendix*, Table S3, germline mutations in other genes, including: 1) 14429G>A (p.Arg4810Lys)

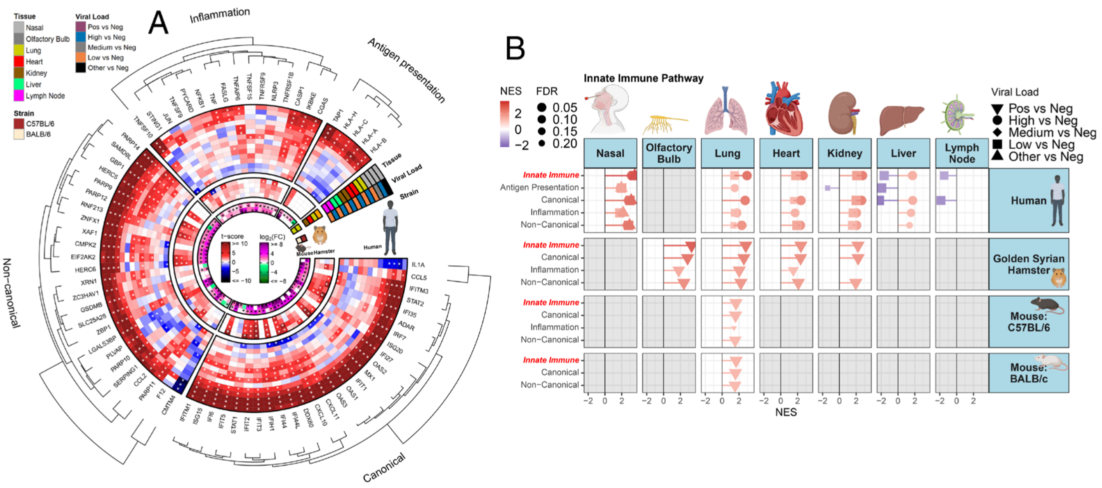

Fig. 2. Mid- and late-stage and innate immune gene expression transcript changes in infected rodent samples and human autopsy tissues from COVID-19 patients. (*A*) Circular heatmap displaying the t-score statistics for specific innate immune genes, comparing SARS-CoV-2 infected hamster tissues, viral load versus negative patient nasopharyngeal and autopsy tissue samples, and $\log_2$-foldchange for SARS-CoV-2 infected C57BL/6 and BALB/c mouse lungs. (*B*) Lollipop plots for custom gene sets determined by fGSEA (FDR < 0.25), ranked by NES.

polymorphisms in the microvascular permeability regulator, *RNF213* lead to MOYA-MOYA disease generating intracranial artery atherosclerosis, systemic vascular diseases (45). This gene, upregulated in nasopharyngeal samples, trends downward in the heart, kidney, and liver (Fig. 2*A*); 2) germline loss-of-function mutations in the little-studied *PLVAP* gene, required for routine maintenance of microvascular permeability and gut barrier function, can cause death from severe diarrhea in infants (22). *PLVAP*, while upregulated in nasopharyngeal samples, is downregulated in heart, lung, liver, and kidney (Fig. 2*A*); 3) germline loss and gain of mutations in, respectively, two noncanonical innate immune genes, *SERPING1* and *F12*, which generate excess complement signaling, are leading causes of HAE, a disorder associated with RAAS-overactivation (10). Further importance of RAAS activation in our data is outlined later below. Patients with HAE have vascular and intestinal leakage and a propensity for thrombotic events (10, 48) as seen in lethal COVID-19 (10, 21). Notably, *SERPING1,* while upregulated in nasopharyngeal samples, is downregulated in the lung, liver, and, to a lesser extent, kidney, while *F12* expression is increased in mediastinal lymph nodes (Figs. 1 and 2).

SARS-CoV-2 Infection Alters Extracellular-Mediated Immunity-Associated Genes. In addition to the above transcriptional changes in innate and intracellular-mediated immunity genes, we also define the effects of SARS-CoV-2 infection on the dysregulation of extracellular-mediated immunity-associated genes. These queries include the categories of cell surface marker and surface receptor signaling, interleukins, cytokines, and class II antigen processing and presentation-related machinery (*SI Appendix*, Table S2).

COVID-19 nasopharyngeal samples are enriched for upregulated innate (*CSF1R, CCR1, CD80/86*) and adaptive (*CD3E/4/8/247*) immune genes (Fig. 3 *A* and *B*). In contrast, mediastinal lymph nodes, a central draining lymph node for the thoracic compartment, show a marked downregulation of CD4- and CD8-associated genes inclusive of cell surface molecules, *CD2/3E/4/8A/247* and T cell receptor signaling (*FYN, ITK, LCK*). Several innate and adaptive genes have differential expression across most tissue sites. *MICB* (NKG2D ligand), which functions as a stress-induced "kill-me" antigen, targeting expressing cells for clearance by natural killer cells (49) is upregulated in most autopsy tissues. *CSF1R* and *CD3E/4* have conserved downregulation across most tissue sites (Fig. 3*A*). CSF1R is the receptor for both CSF and IL-34 and is critical for directing differentiation and proliferation of mononuclear phagocytes, an essential class of highly professional antigen-presenting cells (50), while CD3E/4, T lymphocyte helper T cell genes play key roles in adaptive immune responses (51). Importantly, expression of class II MHC antigen processing- and presentation-related genes are altered with their global upregulation in nasopharyngeal samples contrasting with downregulation in lymph nodes and a mixed expression pattern in other organ sites (Fig. 3*A*). Within these antigen-presentation-associated genes, *CD74* warrants special mention for both its conserved downregulation across the autopsy tissues (Fig. 3*A*) and because of its functional importance in loading and chaperoning peptides for antigen presentation (52).

Given the tissue-specific expression of immune cellular markers and antigen-presentation-associated genes (Figs. 2*A* and 3*A*), we sought to define the expression profile of cytokine and interleukin genes, which are critical regulators of immune cell localization and activation (53, 54). As anticipated, inflammatory interleukins and cytokine genes are upregulated in nasopharyngeal samples (Fig. 3*B*). The autopsy tissues also show a broad pattern of interleukin and cytokine augmentation, most manifest for *CXCL9/10/11*, *CCL2/8*, and *IL15RA* (Fig. 3*A*). CXCL9/10/11 are 3 major Th1-type chemokines, which impart cellular chemotaxis through the CXCR3 receptor on both lymphocytic and monocytic populations. CCL2/8 are potent augmenters of monocytic cell type chemotaxis, with CCL2 having a role in severe SARS-CoV-2 (55). In contrast to the cytokines, which are critical for cellular motility, IL15RA acts as a potent lymphoid and myeloid cell activation inducer with the potential to facilitate an inflammatory milieu (56). Together, these interleukin and cytokine patterns reveal a conserved potentiation of chemotactic gradients in human samples, which are known to attract both lymphocytic and monocytic populations in response to interferon and inflammatory stimuli.

GSEA for the above-conserved patterns of gene perturbation suggests significant directionality in human samples with a striking induction of extracellular mediated immunity gene sets for nasopharyngeal samples (Fig. 3*B*). Interestingly, in the kidney, all gene sets except antigen processing and presentation are enriched, while lung and heart show augmentation of cytokine/interleukin or interleukin alone, respectively (Fig. 3*B*). Both liver and mediastinal lymph nodes show a conserved downregulation of extracellular mediated immunity, which is manifest for all gene sets in mediastinal lymph nodes, while liver has downregulated expression for all above gene sets, except cytokines (Fig. 3*B*).

The above data reveal divergent transcriptional responses in lymphocyte-associated genes and class II antigen processing/presentation in SARS-CoV-2. Additionally, lymphoid organs from patients with severe SARS-CoV-2 present with transcriptional downregulation of adaptive immune-associated genes. These data are validated in our animal models of SARS-CoV-2 infection wherein extracellular mediated immunity genes are increased across all tissue sites in both Syrian hamster and mouse models of SARS-CoV-2 (Fig. 3 *A* and *B*); further, the mouse model lung samples have a pattern more similar to human nasopharyngeal samples, while the Syrian hamster model demonstrates similarity to the human cytokine response (*CCL2/8/10*) across all assayed tissue sites.

RAAS Overactivation by Upstream Immune Genes Tracks with Severe Lethal COVID-19. RAAS signaling normally fluctuates to maintain blood pressure, but overactivation induces severe inflammation, as observed in HAE, to trigger its overlapping features with lethal COVID-19 (10). As others have stressed, no single gene expression alteration causes pathogenic RAAS but rather the imbalanced patterns seen in our data below.

Imbalanced angiotensin axis. Chronic diminution of ACE2 or ACE levels and imbalanced angiotensin (AGT) regulatory axis induce overactivated RAAS and tissue-damaging events. This results from alterations of AGT2 binding to AGTR1/2 receptors producing vasoconstriction, inflammation, fibrosis, tissue damage, edema, and activation of NADPH oxidase, which elevates intracellular ROS levelsmetabolism (*SI Appendix*, Fig. S6 and Table S2). Mechanisms include activating renin (REN) renal secretion to generate AGT1 and cleavage of the latter by ACE1, or in the heart by CMA1 and to act through the MAS1 receptor to trigger the above inflammation consequences (10) Fig. 4*A* and *SI Appendix*, Fig. S6 and Table S2). In our

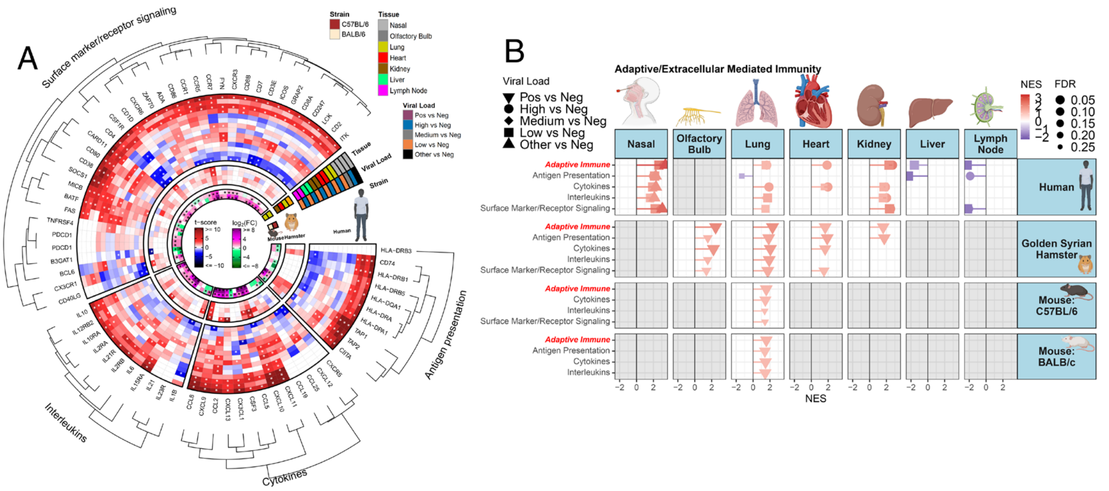

Fig. 3. SARS-CoV-2 infection alters extracellular-mediated immunity-associated gene expression. (*A*) Circular heatmap displaying the t-score statistics for extracellular-mediated immunity-associated genes comparing SARS-CoV-2 infected hamster tissues, viral load versus negative patient nasopharyngeal and autopsy tissue samples, and $\log_2$-foldchange for SARS-CoV-2 infected C57BL/6 and BALB/c mouse lungs. (*B*) Lollipop plots for custom extracellular-mediated immunity-associated gene sets determined by fGSEA (FDR< 0.25) ranked by NES.

autopsy samples, gene expression changes would favor AGTR1 activation over AGTR2/MAS1, resulting in RAAS-activation as reflected by downregulation of *ACE2* and *AGTR2* in the lung, *CSTA* in the heart, and *MAS1* and, to a lesser extent, *AGTR2* in the lymph nodes (Fig. 4*B*).

Overactivation of complement signaling. This key ACE component of RAAS can be induced by the leading HAE germline loss and gain of function mutations, respectively, for two noncanonical innate immune genes, *SERPING1* and *F12* (10, 21). SERPING1 inhibits and F12 facilitates complement activation with accompanying altered downstream regulation of C1QA, C1R, and C1S genes (10, 57, 58). Both *SERPING1* and *F12* are upregulated in nasopharyngeal samples, but *SERPING1* is downregulated in the lung, liver, and to a lesser extent in the kidney, while *F12* is upregulated in the lymph nodes and somewhat in the heart (Fig. 4*B*). *C1QA* is upregulated in the nasopharyngeal, lung, heart, and lymph nodes, and *C1R* in the heart and lymph nodes while downregulated in the liver, and *C5AR1* is upregulated in the lung, heart, and lymph nodes (Fig. 4*B*). Additional germline mutations also induce HAE (59), including *KNG1* (60, 61)*, PLG* (62, 63), *ANGPT1* (64)*, MYOF* (64) (increased in lung and lymph nodes), and *HS3T6* (64) (Fig. 4*B* and *SI Appendix*, Fig. S6 and Table S3). As outlined below, the above gene changes can induce vascular disruption and collaborate with excess fibrosis damage.

PANoptosis. PANoptosis is driven by one of our noncanonical immune genes, *ZBP1,* to mediate multiple modes of cell death (32, 54). *ZBP1* is upregulated in nasopharyngeal samples (Figs. 1 and 4*B*) and retains high expression in the lung, heart, and kidney and, to a lesser extent, in the liver (Figs. 2*A* and 4*B*). ZBP1 induces different PANoptosis death outcomes through differential binding to RIPK1, RIPK3, and MLKL (32, 54) as follows: 1) binding to RIPK1 induces NF-κB-signaling and subsequent TNF and IL6 signaling (32, 54) and *TNF, ZBP1,* and *IL6* expression are coordinately increased in nasopharyngeal samples and to a lesser extent lung, heart, and kidney (Fig. 4*B*). Notably, IL-6, in conjunction with TGF, can also trigger the development of Th17 inflammatory cells. 2) interaction with RIPK3 encoded by *RIPK3*, upregulated in heart and lymph nodes (Fig. 4 *A* and *B*), can activate IFN and NF-κB, cGAS-STING, and mitochondrially-bound-NLRP3 inflammasome signaling, all driving DNA damage to induce dsRNA and dsDNA release into the cell cytosol which drives inflammasome signaling (32). The RIPK3-ZBP1 interaction induces necroptosis through pyroptosis, a process mediated by GSDMs, which function with NLRP3, PYCARD, and caspases to induce swelling and rupture of cell and mitochondrial membranes (32, 54). *NLRP3* is highly expressed in the lung, kidney, and liver, *PYCARD* in the lung and kidney, and *CASP1* in the nasopharyngeal, heart, kidney, and to a lesser extent in the lung and liver (Fig. 4 *A* and *B*). 3) *GSDM/B/C/D* are all significantly upregulated in nasopharyngeal samples and lymph nodes, *GSDMB/C* in the lung, kidney, and heart, and *GSDMD* in the lung and heart (Fig. 4*B*). MLKL-ZBP3 interactions are also central to necroptosis (32, 54). *MLKL* is significantly upregulated in nasopharyngeal, heart, kidney, liver, and lymph node samples (Fig. 4*B*). ZBP1-RIPK3 interaction with FAAD rather than MLKL switches cell death toward apoptosis associated with caspases 3/7/8 (32, 54). *FAAD*, while highly expressed in nasopharyngeal samples, is significantly downregulated in the liver and lymph nodes, while *CASP3* is significantly upregulated in the kidney and highly expressed in all other sites except the lymph nodes. *CASP7/8* is significantly upregulated in the nasopharyngeal, heart, and kidney and to a lesser degree in the lung and liver samples (Fig. 4*B*). Thus, our overall data suggest ZBP1- RIPK3 interactions may drive necroptosis and some apoptosis-inducing PANoptosis in lethal COVID-19.

Fibrin Deposition. Excess fibrin deposition is a vital component of RAAS overactivation interacting with PANoptosis (10, 57, 58, 65, 66). Despite no detectable expression in nasopharyngeal samples, three genes encoding fibrin synthesis enzymes, *FGA/B/G,* are all significantly upregulated in heart and lymph nodes and, to a lesser extent, in lungs (Fig. 4*B*). Serpin protease family gene expression can initiate cycles of excess fibrin deposition turnover and another highly expressed, noncanonical immune gene in nasopharyngeal samples, *SERPINE1,* which encodes a tissue urokinase inhibits fibrinolysis (12, 67–69). This gene retains high expression in lung, heart, and lymph nodes, while *SERPINs C1* and *F2*, encoding plasma thrombin inhibitors (12), while lacking expression in nasopharyngeal samples are significantly upregulated in lymph nodes and, to a lesser extent, lung and heart (Fig. 4*B*). Two other key RAAS over activation components, HA, and bradykinin (BDK), interact with fibrin excess to cause vascular leakiness. HA binds to the HMMR receptor, and increased HA in human plasma correlates with severe COVID-19 while blocking elevated HA in SARS-CoV-2 infected mice decreases mortality (12, 70). Three hyaluronan synthase isoenzyme genes, *HAS1/2/3, HAS2,* are increased in the lung, liver, and kidney, and *HAS3* in lymph nodes. *HYAL2,* which degrades HA (71, 72), while having low expression in nasopharyngeal samples, is significantly decreased in lung, kidney, and liver, while *HMMR* is increased substantially across lung, heart, and liver samples (Fig. 4*B*). BDK production is facilitated by F12 to mediate the conversion of prekallikreins KLK1-15 to kallikreins and their conversion to bradykinin by KNG1, KLKB1, and CPN1, which bind to BDKRB1/2 (73). SPINK5 is a serine protease that inhibits KLKS5/7/14. More nuanced changes in these genes occur in our data, but while having little or no expression in nasal swab samples; *KLK10* is significantly upregulated in the kidney; *KLK11* trends upward in the heart, liver, and kidney, *KLK14* is upregulated in the kidney, liver, and lymph nodes; and *SPINK5* is significantly downregulated in nasopharyngeal samples (Fig. 4*B*).

In conclusion, our data suggest that changes in the expression of upstream essential immune genes are downstream drivers for RAAS overactivation contributing to PANoptosis, excess complement, fibrin, and HA deposition, which induce vascular and other tissue-damaging events in lethal COVID-19. Importantly, these changes suggest severe damage to mediastinal lymph nodes in lethal COVID-19, as explored more deeply below.

Severe SARS-CoV-2 Disrupts Lymphoid Organ Architecture with an Associated Accumulation of Pathogenic Fibroblasts. Immunohistochemistry (IHC) studies validate the above transcriptomic changes and further define severe damage to mediastinal lymph nodes. First, as compared to autopsy controls, there is a small reduction in $CD3^+$ cells (Fig. 5*A*), which is consistent with the downregulation of lymphocyte markers (*CD4, CD8A*) (Fig. 3*A*). Second, our transcriptomic findings of increased expression of complement activation/fibrin deposition-related genes and association with excess fibrin deposition fit with the known recruitment of proliferative, collagen-producing fibroblasts to provide long-term remediation of tissue damage (74). Indeed, there is a striking increase in the prevalence of a cellular

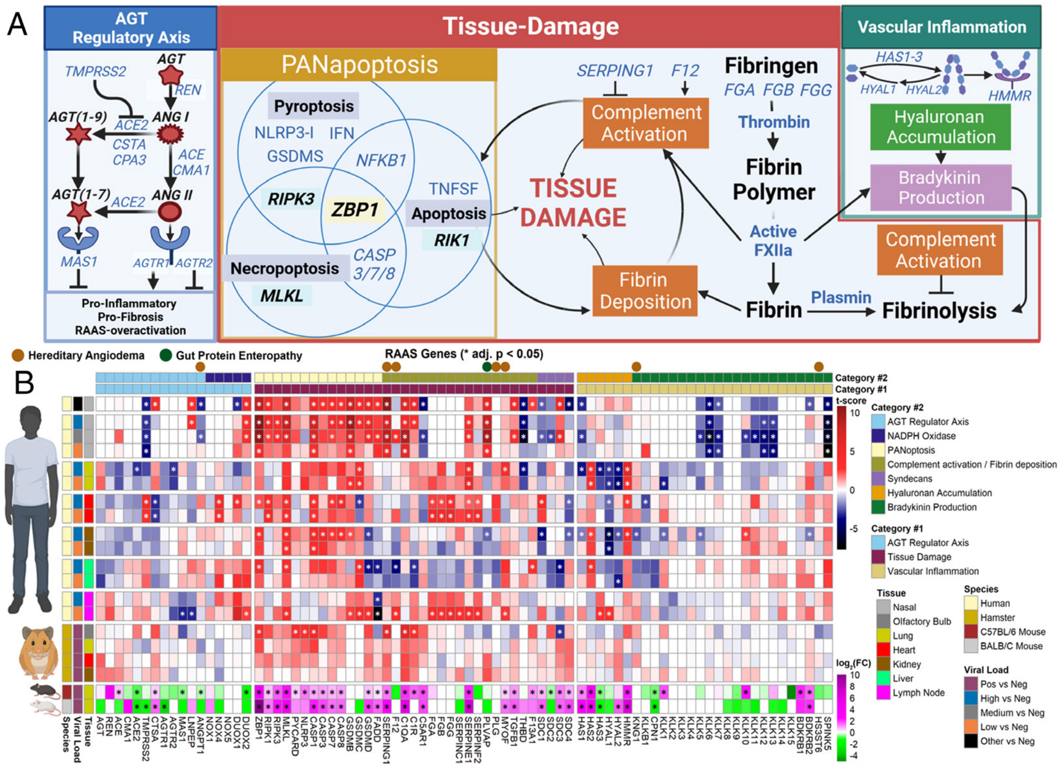

Fig. 4. SARS-CoV-2-infection induces increased transcription of genes involved in RAAS-overaction in human lung, heart, and lymph nodes. (*A*) Schematic summary of RAAS pathway. (*B*) Linear heatmap displaying the *t* score statistics for RAAS target genes comparing SARS-CoV-2 infected hamster tissues, viral load versus negative patient nasopharyngeal and autopsy tissue samples, and $\log_2$-foldchange for SARS-CoV-2 infected C57BL/6 and BALB/c mouse lungs.

population with IHC staining for fibroblast surface protein (FSP) (Fig. 5 *B* and *C*). Third, in association with the above increase in fibroblasts, there is a marked increase in the lymph node samples for both fibrosis percentage (Fig. 5 *D* and *F*) and fiber intensity (Fig. 5 *E* and *F*) as assessed by reticulin staining. This histopathology stain assesses fiber deposition primarily composed of type III collagen and fibronectin and is consistent with fibrotic processes (75–77). Notably, reticulin fibrosis of lymph nodes has been previously reported to have an associated pathophysiology in other disease settings, leading to impaired vaccination responses and cellular replenishment (78, 79). Fourth, as an extension to the above reticular fiber assessment, Mason's trichrome staining for fibrosis reveals a pronounced increase relative to controls (Fig. 5 *G* and *I*). Fifth, consistent with collagen being a significant component of reticulin and trichrome staining, there is an overall increase in collagen fiber width in the lymph node autopsy samples relative to controls (Fig. 5 *H* and *I*). In summary, these IHC data reveal a reduction in $CD3^+$ lymphocytes within the mediastinal lymph node co-occurring with significant increases in fibrosis-associated markers (reticulin, trichrome, collagen) and recruitment of pathogenic fibroblasts.

SARS-CoV-2 Upregulates mtDNA/mtdsRNA-Activated Genes. SARS-CoV-2 inhibition of OXPHOS elevates mROS, stabilizing hypoxia-inducible factor 1 alpha (HIF-1α) (6, 80–82). Upon activation, HIF-1α inhibits OXPHOS and mitochondrial biogenesis, favoring glycolytic metabolism and redirecting carbon molecules away from mitochondrial oxidation toward

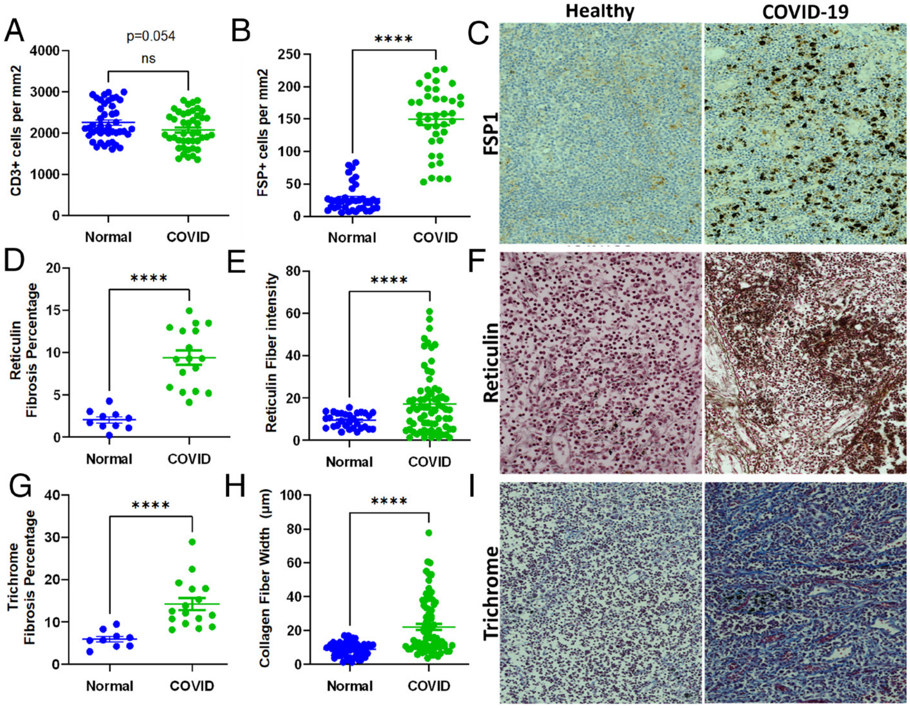

Fig. 5. Severe COVID-19 disrupts organ architecture with an associated accumulation of pathogenic fibroblasts. Mediastinal lymph nodes were obtained from patients without lung disease or from patients who died from COVID-19. 5 regions (at 10× magnification were evaluated from each patient sample and evaluated for (*A*) CD3 (cells/cm^2), (*B*) FSP (cells/cm^2), (c) representative staining of FSP staining, (*D*) reticulin staining and the percentage of area with reticulin staining, (*E*) reticulin fiber intensity, (*F*) representative staining of reticulin staining, (*G*) percentage of fibrosis staining (based on Trichrome staining), (*H*) collagen fiber length, and (*I*) representative staining of Trichrome staining.

nucleic and fatty acid synthesis, thus favoring SARS-CoV-2 biogenesis (81). Elevated mROS also leads to the oxidation and release of mtDNA and mtdsRNA into the cytosol (16, 81–83). Once in the cytosol, these mitochondrial components mimic viral genomes and are detected by sensors of immunostimulatory RNA/DNA (Fig. 6*A*). Cytosolic mtDNA binds to the NLRP3- and AIM2-inflammasomes activating CASP1, which triggers the secretion of interleukins IL-1β and IL-18 and GSDMD-mediated pyroptosis (15, 16). mtDNA also binds TLR9-MYD88, while mtdsRNA binds to EIF2AK2/PKR, TLR3-TRIF, and DDX58-IFIH1-MAVS. Both mtDNA and mtdsRNA bind to ZBP1 and cGAS-STING, leading to the induction of IFN, IRF, NF-κB, and their target genes, activating an innate immune response (81, 83). The binding of mtDNA and mtdsRNA to ZBP1 also triggers PANoptosis (35, 84) (Fig. 6*A*).

In our prior study analyzing bioenergetic changes in the same human and rodent samples, we observed transcriptional inhibition of mitochondrial genes associated with OXPHOS and increased expression of HIF-1α-target genes in COVID-19 nasopharyngeal and heart, kidney, and liver autopsy samples (Fig. 6*B*). Similarly, the COVID-19 lung autopsy samples and infected rodent tissues showed elevated expression of HIF-1α-target genes. OXPHOS suppression in these tissues, due to decreased OXPHOS transcripts and increased HIF-1α activation, likely results in elevated mROS levels and the subsequent release of mtDNA/mtdsRNA, activating an innate immune response. To determine whether cytosolic mtDNA/dsRNA contributed to an activated immune response in these tissues, we examined their presence using our custom gene list (*SI Appendix*, Table S2).

In the SARS-CoV-2-positive nasopharyngeal samples, where immune activation was aided by the presence of viral dsRNAs, we observed the highest upregulation of both mtDNA- and mtdsRNA-activated immune genes among the human samples (80) (Fig. 6*C*). Significantly, in the absence of SARS-CoV-2 RNAs (*SI Appendix*, Table S1), the COVID-19 lung, heart, and kidney autopsy tissues exhibited substantial upregulation of all mtDNA/mtdsRNA-activated innate immune pathways. Consistent with the innate immune data, the mtDNA/mtdsRNA-activated innate immune pathways were only mildly upregulated in the liver, and no significant pathway upregulation was observed in the lymph nodes (Fig. 6 *C* and *D*).

mtDNA/mtdsRNA-activated pathways were also broadly upregulated in infected SARS-CoV-2-positive rodent lungs, with mouse lungs showing a greater extent of upregulation compared to hamster lungs, aligning with the less severe infection observed in hamsters (Fig. 6*C*). Comparable to the human autopsy tissues, the heart and olfactory bulb and to a lesser extent kidney tissues collected from infected hamsters also displayed a considerable upregulation of all the mtDNA/mtdsRNA-activated pathways, in the absence of SARS-CoV-2 transcripts (*SI Appendix*, Table S1). Since no SARS-CoV-2 transcripts were present in the COVID-19 autopsy and hamster brain and visceral tissues, the activation of these immunostimulatory sensors is likely due to the release of mtDNA and mtdsRNA.

At the individual gene level, we observed significant upregulation of the genes encoding for CMPK2, ZBP1, and cGAS, as well as the IRF and NF-κB genes (Figs. 2*B* and 6*D*). Notably, CMPK2, which is the rate-limiting step for mtDNA replication, increases the creation and release of oxidized mtDNA from the mitochondrion in the presence of elevated mROS (13, 38). The upregulation of *CMPK2* in COVID-19 nasopharyngeal, heart, and kidney samples, as well as in rodent lung and visceral tissues, could contribute to the release of mtDNA from these tissues. Consistent with previous reports showing that SARS-CoV-2 ORF10 represses MAVS to help the virus evade the innate immune response (Figs. 2*B* and 6*D*), we observed a robust downregulation of *MAVS* in SARS-CoV-2-positive nasopharyngeal samples and hamster lungs (85). Additionally, the gene encoding EIF2AK2/PKR, which senses viral and mitochondrial dsRNA, was upregulated in all tissues except for the lymph nodes, where it was downregulated (Fig. 6*D* and *SI Appendix*, Figs. S8 and S9*A*). Since EIF2AK2/PKR plays a crucial role in the ISR, its consistent upregulation suggests increased activation of the ISR in these tissues (86, 87).

SARS-CoV-2 Activates the ISR and Unfolded Protein Response (UPR) in Several Tissues. While acute activation of the UPR and ISR helps cells adapt to environmental stressors and promotes cell survival, chronic signaling can lead to inflammation and cell death (*SI Appendix*, Fig. S8). Environmental stresses initiate the ISR through four specialized kinases: EIF2AK1/HRI detects mitochondrial UPR response (UPR^{MT}) activation signaled through the cleavage and binding of DELE1, EIF2AK2/PKR detects dsRNA, EIF2AK4/GCN2 senses amino acid deprivation and oxidative stress, and EIF2AK3/PERK responds to the accumulation of unfolded/misfolded proteins in the endoplasmic reticulum (UPR^{ER}) (86, 87). Activation of EIF2AK1-4 triggers the phosphorylation of eIF2α, leading to the activation of transcription factors ATF4/5 and their downstream target genes, including cytokines and death factors (87, 88) (*SI Appendix*, Fig. S8). UPR^{ER} activation also upregulates genes involved in ER-homeostasis and cytokines/death factors (88), while the UPR^{MT} upregulates antioxidant and mitochondrial maintenance genes (89, 90).

The ISR was significantly activated in all the COVID-19 autopsy tissues except the lymph nodes (*SI Appendix*, Fig. S9 *A* and *B*). Activation was highest in the lung and nasopharyngeal tissues, followed by the heart, kidney, and, to a lesser extent, the liver. The $UPR^{MT/ER}$ was upregulated in the human lung, and the UPR^{MT} was downregulated in the heart and

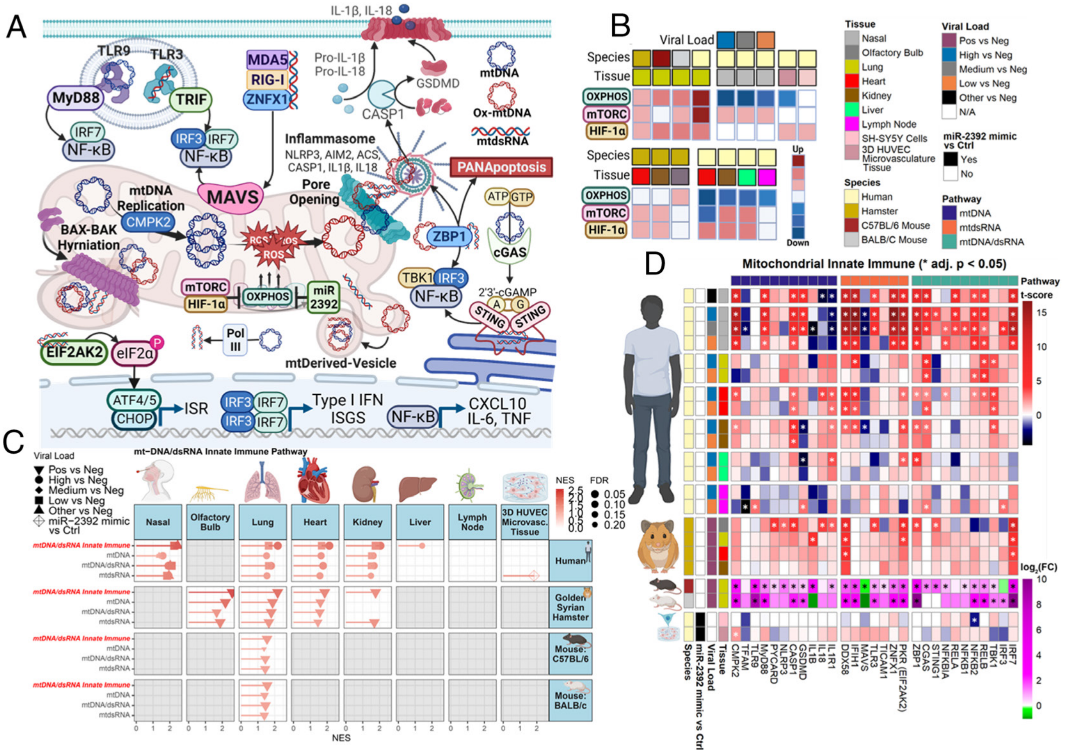

Fig. 6. SARS-CoV-2 infection upregulates mtDNA/mtdsRNA-activated genes despite the absence of viral transcripts. (*A*) Schematic summary of mtDNA/mtdsRNA-activated pathways. (*B*) Graphical representation of findings from Guarnieri et al. (80). (*C*) Lollipop plots for statistically significant changes determined by fGSEA, ranked by NES, and (*D*) Linear heatmaps displaying the t-score statistics for mtDNA/mtdsRNA-activated genes SARS-CoV-2 infected hamster tissues, viral load versus negative patient nasopharyngeal and autopsy tissue samples, miR-2392-expressing 3D-HUVEC-MT cells, and log_2-foldchange (FC) for SARS-CoV-2 infected C57BL/6 and BALB/c mouse lungs.

upregulated in the lymph nodes (*SI Appendix*, Fig. S10 *A* and *B*). In the infected rodents, the ISR and UPR^{ER} were upregulated in the mouse lungs, with the ISR also upregulated to a lesser extent in the hamster lung, kidney, and heart (*SI Appendix*, Fig. S10). Consistent with chronic stress signaling, the ISR and UPR were most upregulated in the autopsy lung samples, followed by the mouse and hamster lung samples. For the visceral tissues, the human heart and kidney displayed increased transcription of ISR-target genes compared to their hamster counterparts, suggesting increased ISR activation with COVID-19 progression in these tissues.

At the individual gene level, the genes encoding for EIF2AK4/GCN2 and EIF2AK1/HRI, which sense mitochondrial dysfunction, were upregulated in the human autopsy tissues (*SI Appendix*, Fig. S9*B*). Genes encoding PGC-1α, which regulates mitochondrial biogenesis and quality control (91), and GPX4, AIFM2, PARL, and STARD7, which detoxify lipid peroxidation and inhibit ferroptosis (92, 93), were strongly downregulated in the human heart and kidney autopsy tissues. Their downregulation would elevate mROS, contributing to the innate immune response in these tissues (*SI Appendix*, Fig. S10*A*).

miR-2392 inhibits OXPHOS transcripts and enhances the expression of immune genes. SARS-CoV-2-induces the expression of microRNA-2392 (miR-2393), which binds mtDNA and is associated with impaired transcription of both nuclear DNA (nDNA)- and mtDNA-encoded OXPHOS genes (80, 94). Previously, we showed that expression of a miR-2392 mimic in three-dimensional human umbilical vein endothelial cell microtissue (3D-HUVEC-MT) robustly downregulated the expression of nDNA OXPHOS genes (80) (Fig. 6 *A* and *B*). Expanding on these finds, we observed that miR-2392 significantly upregulated the innate immune (*SI Appendix*, Fig. S11 *A* and *B*), ISR, and mtdsRNA-activated pathways and the expression of *CMPK2* (Fig. 6*C*). This indicates that miR-2392 can contribute to the overactivation of the innate immune response through OXPHOS inhibition. Additionally, expression of miR-2392 in 3D-HUVEC-MT downregulated antioxidant and autophagic ISR-target genes, which could further contribute to miR-2392-induced mitochondrial dysfunction (*SI Appendix*, Figs. S10 and S11).

In conclusion, our data support the hypothesis that SARS-CoV-2-induced mitochondrial dysfunction, mediated via OXPHOS inhibition, HIF-1α activation, and the expression of miR-2393, elicits the release of mitochondrial mtDNA/mtdsRNA, contributing to the cytokine storm (Fig. 6). Significant upregulation of mtDNA/mtdsRNA-activated immune pathways was observed in COVID-19 nasopharyngeal, heart, lung, kidney, and rodent tissues. In all SARS-CoV-2-positive tissues, except for the lymph nodes, we observed increased expression of *EIF2AK2/PKR* and upregulation of ISR pathways, which, when chronically activated, promote inflammation and cell death (*SI Appendix*, Figs. S9–S11). This was particularly evident in the autopsy lung samples, followed by the mouse and hamster lung samples. Finally, consistent with the initiation of cell death pathways downstream of mtDNA/mtdsRNA release and chronic ISR activation, the upregulation of these pathways correlated with increased expression of *ZBP1* and upregulation of PANoptosis pathways (Fig. 4) in all tissues except for the lymph nodes. Since no SARS-CoV-2 transcripts were present in the COVID-19 autopsy and hamster brain and visceral tissues, activation of the mtDNA/mtdsRNA-activated immune pathways, ISR, and PANoptosis pathways must be attributed in part to the release of mtDNA and mtdsRNA and activation of diffusible factors that act on target tissues. These data underscore the critical role of SARS-CoV-2-induced mitochondrial dysfunction in contributing to the cytokine storm and COVID-19 pathogenesis.

PBMCs and Whole Blood Samples from Early and Later Variants of SARS-CoV-2 Display Comparable Immune Responses. PBMCs from patients infected with Alpha and Omicron strains, as well as whole blood from individuals infected during the Pre-Delta period (before July 1, 2021) and the Delta period (July 1, 2021, to December 31, 2021) with SARS-CoV-2, were analyzed (see *SI Appendix*, Tables S4 and S5 for participant clinical characteristics and genotype summaries for whole blood samples). These peripheral compartment-derived samples display robust upregulation of the canonical innate immune, RAAS, and mtDNA/mtdsRNA-activated innate immune genes, comparable to the human nasopharyngeal samples (Fig. 7*A* and *SI Appendix*, Fig. S12). Additionally, 18 of the 21 noncanonical immune genes upregulated in the SARS-CoV-2 positive nasopharyngeal samples, as well as genes involved in the inflammasome and NF-κB signaling, are also significantly upregulated in the PBMCs and blood samples collected from SAR-CoV-2 infected individuals (*SI Appendix*, Fig. S12). Eight genes show consistent upregulation in our SARS-CoV-2 positive tissues and PBMCs collected from Alpha- and Omicron-infected individuals and blood samples collected from the Pre-Delta and Delta periods (Fig. 7*B*). These genes are five mitochondrial-associated innate immune genes, *CMPK2, CGAS, ZBP1, EIF2AK2,* and *GDF15.* Also elevated are *MICB*, which encodes an antigen for clearance by natural killer cells (49); and cytokines *CXCL10* and *CXCL11*, associated with COVID-19 severity (41) (Fig. 7*B*). In summary, we observed significant upregulation of mtDNA/mtdsRNA-activated immune response with associated induction of EIF2AK2/PKR and ISR pathways. These events then facilitate the acquisition of a dysfunctional RAAS pathway state, which underlies the tissue damage response observed in COVID-19 pathogenesis (Fig. 7*C*).

PBMC and blood from individuals infected with the early variant display a robust downregulation of genes involved in the adaptive and extracellular mediated immunity (Fig. 7), which generally recapitulates the response of the autopsy lymph nodes (Fig. 3*A* and *SI Appendix*, Fig. S12). In PBMCs, genes involved in class II antigen processing and presentation (*HLA-DRA, HLA-DRB1, HLA-DQA1*), TCR signaling (*LCK, FYN*), and lymphocyte state (*CD8A, CD8B, CD4, CD3E,* and *CCR7*) are significantly downregulated in Alpha-infection relative to healthy controls (*SI Appendix*, Fig. S12). In contrast, the Omicron-infection is associated with an overall muted transcriptional response, with the notable exception of monocytic chemotaxis (*CCL2, CCL8*) augmentation (*SI Appendix*, Fig. S12). These data reveal strain-specific behavior in the peripheral compartment, with the caveat that we cannot define whether these are based on the virus alone or a host viral interaction mediated by prior vaccination or infection. In aggregate, genes of innate immune, RAAS, and mtDNA/mtdsRNA in PBMCs are similarly upregulated in Alpha and Omicron variant infections; however, extracellular mediated immunity-related genes show divergent expression patterns wherein Alpha downregulates while Omicron upregulates these genes.

Discussion

Our present study offers insights that increase understanding of the inflammation dynamics that drive lethal outcomes for patients infected by SARS-CoV-2. First, we expand the dimensions of cytokine storm by linking alterations in canonical with an upstream role for noncanonical IFN-signaling genes to induce signaling overactivity of the RAAS pathway. Our study is informed by evaluating the effects of several genes for which germline mutations cause HAE, an inflammatory syndrome with tissue damage widely overlapping that seen in severe COVID-19 (10, 48). The dynamics for germline loss and gain-of-function mutations are especially revealing for *SERPING1* and *F12*, each resulting in excess complement activity to induce RAAS overactivation components, increasing fibrin deposition. These findings point to the mechanism by which COVID-19 induces systemic vascular leakage, loss of gut wall integrity, and thrombosis. Findings for rare germline mutations in genes such as *PVLAP*, which produces a similar loss of vascular and gut integrity, cause a similar transcriptional profile as COVID-19. Also, we reveal a role in COVID-19 for *ZNFX1*, a little-studied gene for which rare germline mutations render patients incapable of mounting a response to pathogens. For RAAS overactivation, we emphasize, as have others (48), that changes for expression of any one gene alone cannot be relied upon to judge overall or even a component of RAAS overaction. Instead, integrating many genes and their ramifications for pathway signaling must be utilized to demonstrate an imbalance in gene expression driving abnormal RAAS activation.

Second, our study focuses on essential roles for multiple proteins encoded that shuttle from the nucleus to mitochondria during viral infection to foster activation of inflammasome signaling (6, 13–17). Importantly, this signaling occurs when the mitochondrion is damaged by mROS accumulation. Key genes include *ZNFX1, CMPK2,* and our noncanonical innate immune genes functioning as RAAS components, including *GSDMB, XAF1,* and *ZBP1.* The roles of these latter three genes in inducing multiple modes of cell death likely play an integral part in lethal COVID-19. These data link the response dynamics of the host to RAAS-overactivation and the mitochondrial ISR, as well as inflammation and cell death. Changes in ISR gene expression are related to mitochondrial dysfunction through specialized kinases, including EIF2AK1/HRI, which detects the UPR^{MT} via OMA1 activation and DELE1 cleavage, EIF2AK2/PKR, which detects dsRNA, and EIF2AK4/GCN2 which senses amino acid deprivation and oxidative stress (86, 87). OXPHOS inhibition activates HIF-1α via elevated mROS production, triggering the oxidation and release of mtDNA/mtdsRNA into the cytosol and activating immunostimulatory RNA/DNA sensors.

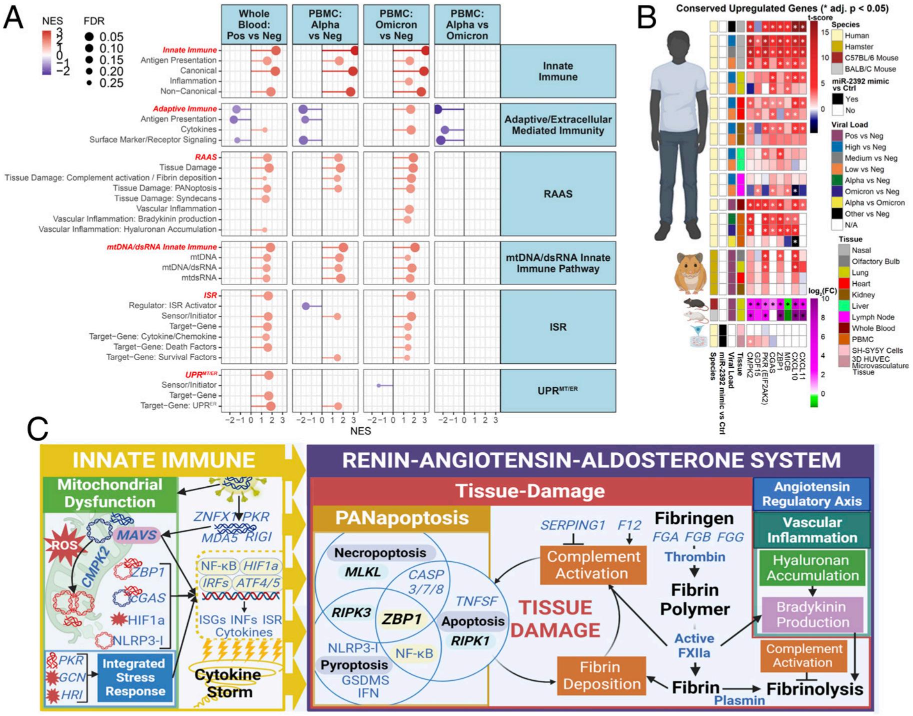

Fig. 7. Transcript changes in PBMCs (Alpha and Omicron) and whole blood (Pre-Delta and Delta) display comparable immune responses. (*A*) Lollipop plots for statistically significant changes in custom gene sets determined by fGSEA for Whole blood and PBMCs ranked by NES. (*B*) Linear heatmap displaying the t-score statistics for conserved upregulated genes comparing PBMCs collected from SARS-CoV-2-Alpha and SARS-CoV-2-Omicron-infected patients versus non-infected patients. (*C*) Schematic summary figure of mtDNA/mtdsRNA-activated immune response with associated induction of EIF2AK2/PKR and ISR pathways driving dysfunctional RAAS pathway state.

In this study, we investigated the intricate interplay between SARS-CoV-2 infection, mitochondrial dysfunction, and ensuing immune responses. Transcriptomic analysis revealed robust inhibition of both nDNA- and mtDNA-encoded OXPHOS genes by SARS-CoV-2, mediated by viral proteins ORF8 and ORF10, alongside the induction of miR-2392 (80–82, 85). This inhibition results in heightened mROS, activation of HIF-1α, and a metabolic shift toward glycolysis, facilitating viral replication (80–82). Concurrently, SARS-CoV-2 viral proteins ORF3a and E elevate mitochondrial $Ca2^+$ and ROS levels, triggering the release of mtDNA and mtdsRNA (16). These mitochondrial components stimulate innate immune responses, evident in elevated circulating mtDNA and proinflammatory cytokines such as IL-1β, correlating with disease severity in COVID-19 patients (95–97).

We observed significant upregulation of mtDNA/mtdsRNA-activated immune pathways in COVID-19 nasopharyngeal, heart, lung, kidney, and rodent tissues. In all SARS-CoV-2-positive tissues, except for the lymph nodes, we observed increased expression of *EIF2AK2/PKR* and upregulation of ISR pathways, particularly evident in the autopsy lung samples, followed by the mouse and hamster lung samples. Consistent with the initiation of cell death pathways downstream of mtDNA/mtdsRNA release and chronic ISR activation, the upregulation of these pathways correlated with increased expression of *ZBP1* and upregulation of PANoptosis pathways in all tissues except for the lymph nodes. Since no SARS-CoV-2 transcripts were present in the COVID-19 autopsy and hamster brain and visceral tissues, activation of the mtDNA/mtdsRNA-activated immune pathways, ISR, and PANoptosis pathways could be attributed in part to the release of mtDNA and mtdsRNA and activation of diffusible factors that act on target tissues.

These findings underscore the pivotal role of SARS-CoV-2-induced mitochondrial dysfunction in driving the cytokine storm and COVID-19 pathogenesis. Moreover, the data suggest that prolonged mitochondrial dysfunction can sustain immune responses independently of viral RNAs, potentially contributing to persistent inflammation associated with long COVID. Therapeutic strategies targeting mitochondrial dysfunction, such as detoxifying mROS or improving mitochondrial OXPHOS, may mitigate these effects. Indeed, interventions using transgenic and pharmacological mitochondrially-targeted antioxidants in SARS-CoV-2-infected cells (6) and animal models (82) showed promising results in reducing mtDNA circulation, inflammatory cytokine levels, and expression of mtDNA/mtdsRNA-activated innate immune genes, thereby decreasing disease severity. However, further research is essential to determine the efficacy and safety of these therapies in human long COVID cases.

Third, the clinical significance of our transcriptomic findings in mediastinal lymph nodes is confirmed by demonstrating fibrosis with associated excess reticulin and collagen deposition (Fig. 5), which has a known association with lymphoid organ architectural changes as reported previously (98–101). General lymphoid organ dysregulation in severe COVID-19 has been described previously in reports that define lymphocyte depletion broadly (102–104), including T-follicular cell helper deficiencies (105, 106), fibrin deposition (107), and germinal center disruption (107–110) further elucidating the basis of COVID-19 lymphopenia (Fig. 3). Activation of the acute fibrin response associated with fibrosis in the lymphoid organs may be analogous to the long-term dynamics in wound healing (77), which we correlate with overactivated RAAS signaling. Hence, damage to the mediastinal lymph nodes could be critical for the defective adaptive immune response that severely comprises immune function, leading to lethal outcomes in COVID-19. Finally, our data may illuminate the persistent, unresolved lymphoid organ dysfunction observed in PASC or "long COVID." For example, a recent study that tracked patients with PASC found dysfunctional B- and T-cell responses with elevated Type I IFN responses still present at 8 mo postacute disease resolution (111).

While the innate and adaptive immune responses to SARS-CoV-2 are diverse and complex, there is increasing evidence of the integration between various cellular compartments in mounting a unified defense against SARS-CoV-2 infection. We have found that SARS-CoV-2 infection inhibits mitochondrial proteins that block the transcription of mitochondrial genes encoded in both the nuclear and mitochondrial DNAs (80). This mitochondrial inhibition stimulates the induction of the non-canonical innate immune, *CMPK2*, which regulates the rate-limiting step of mtDNA replication, which, in conjunction with mROS, results in the release of mtDNA through the mitochondrial permeability pore to activate the inflammasome and cGAS-STING pathways (16). This linkage between mitochondrial dysfunction and the innate immune system links to these dynamics and SARS-CoV-2 induction of ZNFX1 and ZBP1. The SARS-CoV-2 hyper-induction of ZNFX1 activates the interferon response by interacting with MAVS (31), and ZBP1 binds mtDNA and the telomeric-repeat-containing RNAs (TERRA), and the TERRA-bound ZBP1 oligomerizes into filaments on the outer mitochondrial membrane to activate MAVS (35). Thus, the innate immune system links nuclear telomeres with cytosolic nucleic acid receptors and mitochondrial nucleic acid signaling.

In summary, we have defined unifying gene expression dynamics of innate and adaptive immunity that results from SARS-CoV-2 infection. Utilizing pathway analyses and leading-edge genes from our sequencing data, we developed strong hypotheses for causality and identified genes previously unstudied in COVID-19 pathogenesis, thus seeding future experiments. Our histopathology findings, as demonstrated in Fig. 5, substantiate critical findings from our transcriptional analyses, showing fibrosis and immune alterations in thoracic lymph nodes and validating our gene and pathway predictions in both human and rodent models. In total, these data suggest that overactivation of RAAS signaling and mitochondrially mediated inflammation activation holistically comprise the cytokine storm that causes lethal COVID-19.

Limitations of the Study

This study has several limitations. First, some of the clinical components of the study were designed retrospectively. Consequently, COVID-19 and control groups are not matched for demographic variables, comorbidities, or in-hospital treatments. Second, the transcriptomic results alone must rely on correlational interpretation without demonstrating causation. However, orthogonal data derived from rodent SARS-CoV-2 infection models provide a measure of validation for key findings uncovered by these correlational studies. Furthermore, quantitative IHC analyses confirm cellularity and architecture changes, which are directly correlated with our transcriptomic data. Indeed, the key conclusions we draw require and invite validation in follow-up studies in larger cohorts.

Materials and Methods

RNA Sequencing Approach and Study Design. To determine the effects of SARS-CoV-2 infection on the transcriptome, we calculated relative expression levels of host genes in RNA-seq data from 735 nasopharyngeal samples and 40 autopsy cases from SARS-CoV-2 positive and negative individuals as previously described (80). We then compared infected and control subjects' gene expression levels using a curated set of immune genes (*SI Appendix*, Table S2). Human sample collection related to the above was conducted in a Tissue Procurement Facility that operates under Institutional Review Board (IRB) approved protocol and follows guidelines set by the Health Insurance Portability and Accountability Act. Experiments using samples from human subjects were conducted in accordance with local regulations and with the approval of the IRB at the Weill Cornell Medicine. The autopsy samples were collected under protocol 20-04021814, as detailed previously (112). Hamster (4), mouse (113), and PBMCs from COVID-19 patients infected with the Alpha (114) or Omicron (115) strains studies extended the conclusions. Whole blood sample RNAseq data were derived from PAXgene specimens collected from 221 Military Health System beneficiaries with SARS-CoV-2 infection who enrolled in the Epidemiology, Immunology, and Clinical Characteristics of Emerging Infectious Diseases with Pandemic Potential (EPICC) study (116). The EPICC study was approved by the Uniformed Services University Institutional Review Board (IDCRP-085) and all study participants provided consent when enrolled in the study (116). This study was conducted following good clinical practice and according to the Declaration of Helsinki guidelines. All animal experiments were performed as previously described using approved standard operating procedures and safety conditions for SARS-CoV-2 (4, 113). For all experiments, preprocessing was blinded until the higher-order analysis, which involved determining fold-change values, t-scores, pathway analysis, and statistics. No data were excluded from any of the analyses. See *SI Appendix*, Materials, and Methods for a detailed description of sample collection and RNA sequencing analysis methodology.

Transfection of 3D HUVEC Tissue and SH-SY5Y with miR-2392 Mimics. Mature human 3D microvascular tissue models were grown by seeding human umbilical vein endothelial cells (HUVECs) into a collagen/matrigel mixture as previously described (80, 94). Briefly, HUVECs were first grown in EGM Endothelial Cell Growth Medium, then cells (1×10^6/mL) were embedded into a collagen/matrigel mixture. Microvessels were grown for 7 d in EGM-2 Endothelial Cell Growth Medium with 50 nM Phorbol-12-myristate-13-acetate: (PMA) to form tubular microvessels prior to irradiation.

These tissue models were used to study vascular changes associated with miR-2392 mimics. The 3D HUVEC tissues were incubated with the miR-2392 mimics or control lentivirus particles (MOI 1) for 48 h. The tissue constructs used for miR-2392 mimics were dissolved in TRIzol 48 h posttransfection without any fixation or homogenization.

Cell culture, RNA-seq analysis, and data processing of miR-2392 mimic experiments in SH-SY5Y cells were conducted as described previously (94).

Mediastinal Lymph Node Histopathology. Lymph nodes were fixed via 10% neutral buffered formalin inflation, sectioned, and fixed for 24 h before processing and embedding into paraffin blocks. Freshly cut 5-µm sections were mounted onto charged slides. Slides were stained using FSP1 antibody, hematoxylin, and eosin, reticulin, and Masson's Trichrome according to standard protocol. Four 20× regions were randomly selected from each slide the color deconvolution2 algorithm for ImageJ, and cellular trichrome-rich areas were manually selected and measured for pixel area (cellular areas on red deconvolution, trichome on blue deconvolution). The total image pixel area was used to determine the percent fibroblast-rich trichrome-positive zones.

Disclaimer. The opinions expressed in this article are those of the authors and do not reflect the views of the NIH, the Department of Health and Human Services, and the United States Government. The contents of this publication are the sole responsibility of the author(s) and do not necessarily reflect the views, opinions, or policies of Uniformed Services University of the Health Sciences (USUHS); the Department of Defense (DoD); the Departments of the Army, Navy, or Air Force; the Defense Health Agency: the Henry M. Jackson Foundation for the Advancement of Military Medicine Inc; the NIH. Mention of trade names, commercial products, or organizations does not imply endorsement by the U.S. Government. The investigators have adhered to the policies for the protection of human subjects as prescribed in 45 CFR 46.

Data, Materials, and Software Availability. The published article includes all datasets generated and analyzed during this study. Processed bulk RNA-seq data for the human-related data from the nasopharyngeal and autopsy data is available online with dbGaP Study Accession No.: phs002258.v1.p1 and online here at: https://www.ncbi.nlm.nih.gov/projects/gap/cgi-bin/study.cgi?study_id=phs002258.v1.p1 (117) and also https://covidgenes.weill.cornell.edu/. The murine RNA-seq data are deposited on the gene expression omnibus (GEO) repository with Accession No. GSE221510 and can be found here: https://www.ncbi.nlm.nih.gov/geo/query/acc.cgi?acc=GSE221510 (118). Additionally, the murine RNA-seq data were also deposited in the NCBI BioProject database (https://www.ncbi.nlm.nih.gov/bioproject/) under the BioProject accession number PRJNA803057. The hamster RNA-seq data are also deposited on the GEO repository with Accession No. GSE203001 and can be found here: https://www.ncbi.nlm.nih.gov/geo/query/acc.cgi?acc=GSE203001 (119). The RNA-seq data from the miR-2392 mimic 3D HUVEC tissue model data is available via the NASA Open Science Data Repository's (OSDR) Biological Data Management Environment (https://osdr.nasa.gov/bio/repo) with Accession No.: OSD-577 and 10.26030/rs3g-e189 (120). This study did not generate new unique reagents. RNA-seq data will be deposited. All other data are included in the manuscript and/or *SI Appendix*. Previously published data were used for this work (4, 113–116).

ACKNOWLEDGMENTS. This work was supported by the Division of Intramural Research, NIAID, NIH grant to S.M.B., and DOD W81XWH-21-1-0128 grant awarded to D.C.W. This work was also supported, in whole or in part, by the Bill & Melinda Gates Foundation Grant# INV-046722 awarded to D.C.W. Under the grant conditions of the Foundation, a Creative Commons Attribution 4.0 Generic License has already been assigned to the Author Accepted Manuscript version that might arise from this submission. This work was also supported by awards from the Adelson Medical Research Foundation, Hodson Scholar Foundation and Samuel Waxman Research Foundation (S.B.B), and The Evelyn Grollman Glick Scholar Award (M.J.T.). Additional related grants include, Defense Health Program (HU00012020067 and HU00012120103), the National Institute of Allergy and Infectious Disease (HU00011920111), and the USU RESPONSE award (HU00012020070). The EPICC protocol was executed by the Infectious Disease Clinical Research Program (IDCRP), a Department of Defense (DoD) program executed by the Uniformed Services University of the Health Sciences (USUHS) through a cooperative agreement by the Henry M. Jackson Foundation for the Advancement of Military Medicine, Inc. (H.J.F.). This project has been funded in part by the National Institute of Allergy and Infectious Diseases at the NIH, under an interagency agreement (Y1-AI-5072). We thank the members of the EPICC COVID-19 Cohort Study Group for their many contributions in conducting the study and ensuring effective protocol operations. We thank the members of the EPICC COVID-19 Cohort Study Group for their many contributions in conducting the study and ensuring effective protocol operations. The following members were all closely involved with the design, implementation, and/or oversight of the study and have met group authorship criteria for this manuscript: Alexander T. Augusta Military Medical Center, VA: Derek Larson; Uniformed Services University of the Health Sciences, Bethesda, MD: Margaret Sanchez, Ed Parmelee, Julia Rozman, Amber Michel, Robert O'Connell, Andrew

Snow, Paul Blair; Madigan Army Medical Center, Joint Base Lewis McChord, WA: Christopher Colombo, Rhonda Colombo; Naval Medical Center Portsmouth, Portsmouth, VA: Tahaniyat Lalani; Naval Medical Center San Diego, San Diego, CA: Ryan Maves, Catherine Berjohn; Tripler Army Medical Center, Honolulu, HI: Milissa Jones; U.S. Air Force School of Aerospace Medicine, Wright-Patterson, OH: Anthony Fries; Walter Reed National Military Medical Center, Bethesda, MD: Anuradha Ganesan; William Beaumont Army Medical Center, El Paso, TX: Rupal Mody.

Author affiliations: [a]COVID-19 International Research Team, Medford, MA 02155; [b]Department of Oncology, The Sidney Kimmel Comprehensive Cancer Center, Johns Hopkins University School of Medicine, Baltimore, MD 21287; [c]The Children's Hospital of Philadelphia, Philadelphia, PA 19104; [d]Center for Mitochondrial and Epigenomic Medicine, The Children's Hospital of Philadelphia, Philadelphia, PA 19104; [e]Pathology and Laboratory Medicine, Weill Cornell Medicine, New York, NY 10065; [f]School of Medicine, University of Nottingham, Derby DE22 3DT, United Kingdom; [g]Icahn School of Medicine, Mount Sinai, New York, NY 10023; [h]Weill Cornell Medicine, New York, NY 10065; [i]Infectious Disease Clinical Research Program, Department of Preventive Medicine and Biostatistics, Uniformed Services University, Bethesda, MD 20814; [j]Henry M. Jackson Foundation for the Advancement of Military Medicine Inc., Bethesda, MD 20817; [k]Department of Anatomy, Physiology & Genetics, Uniformed Services University, Bethesda, MD 20814; [l]University of North Carolina, Chapel Hill, NC 27599; [m]Department of Biomedical and Health, The Children's Hospital of Philadelphia, Philadelphia, PA 19104; [n]The University of Pennsylvania, Philadelphia, PA 19104; [o]University of Texas Monroe Dunaway Anderson Cancer Center, Houston, TX 77030; [p]University of Texas Medical Branch, Galveston, TX 77555; [q]Innate Immunity and Pathogenesis Section, Laboratory of Neurological Infections and Immunity, National Institute of Allergy and Infectious Diseases, NIH, Rocky Mountain Laboratories, Hamilton, MT 59840; [r]Fogarty International Center, NIH, Bethesda, MD 20892; [s]Cures Within Reach, Chicago, IL 60602; [t]Champions Service, Computational Sciences Support Network, Multi-Tier Assistance, Training, and Computational Help Track, NSF's Advanced Cyberinfrastructure Coordination Ecosystem: Services and Support, Carnegie-Mellon University, Pittsburgh, PA 15213; [u]Center for Translational Data Science, University of Chicago, Chicago, IL 60615; [v]Clever Research Lab, Springfield, IL 62704; [w]Morehouse School of Medicine, Atlanta, GA 30310; [x]Center for Radiological Research, College of Physicians and Surgeons, Columbia University, New York, NY 19103; [y]Laboratory of Immunometabolism, Department of Genetics, Evolution, Microbiology and Immunology, Institute of Biology, University of Campinas, Campinas, São Paulo, Brazil 13083-862; [z]New York Genome Center, New York, NY 10013; [aa]Center for Metabolic Biology, Bioinformatics and Computational Biology, and Genetics Development, and Cell Biology, Iowa State University, Ames, IA 50011; [bb]Center for Bioinformatics and Computational Biology Iowa State University, Ames, IA 50011; [cc]Center for Genetics Development, and Cell Biology Iowa State University, Ames, IA 50011; [dd]Department of Pediatrics, University of Pennsylvania Perelman School of Medicine, Philadelphia, PA 19104; [ee]Stanley Center for Psychiatric Research, Broad Institute of Massachusetts Institute of Technology and Harvard, Cambridge, MA 02142; [ff]Blue Marble Space Institute of Science, Seattle, WA 98104; [gg]McGowan Institute for Regenerative Medicine and Center for Space Biomedicine, Department of Surgery, University of Pittsburgh, Pittsburgh, PA 15219; [hh]Division of Human Genetics, Department of Pediatrics, University of Pennsylvania, Philadelphia, PA 19104; and [ii]Van Andel Institute, Grand Rapids, MI 49503

Author contributions: M.J.T., J.W.G., A. Beheshti, D.C.W., and S.B.B. designed research; M.J.T., J.W.G., A.C., J.F., A. Borczuk, S.S., J.K., J.P., D.B., C.M., J.F., Y.B., M.T.H., N.J.M., V.K.B., E.A.M., S.A.T.-B., E.J.A., W.A.S., R.J.D., J.C.S., P.M.M.-V., C.E.M., D.T., R.E.S., A. Beheshti, and S.B.B. performed research; M.J.T., J.W.G., J.A.H., H.C., J.A., S.A.R., N.J.E., B.A., J.G.C., M.P.S., D.T., T.B., C.D., K.B., G.A.W., K.A.J., T.L., D.G.M., A.A., Y.E.S.A., A.Z.O., Z.C., J.D., W.P., M.R.E., S.M.B., M.K.J., N.S.T., K.B.C., V.Z., R.M., P.G., S.P., E.S.W., D.T., A. Beheshti, D.C.W., and S.B.B. analyzed data; P.M.M.-V., S.P., E.S.W., D.T., and R.E.S. participated in regular discussions; and M.J.T., J.W.G., A. Beheshti, D.C.W., and S.B.B. wrote the paper.

1. E. Dong, H. Du, L. Gardner, An interactive web-based dashboard to track COVID-19 in real time. *Lancet Infect. Dis.* **20**, 533–534 (2020), 10.1016/S1473-3099(20)30120-1.
2. D. L. Ng *et al.*, A diagnostic host response biosignature for COVID-19 from RNA profiling of nasal swabs and blood. *Sci. Adv.* **7**, eabe5984 (2021), 10.1126/sciadv.abe5984.
3. M. Liao *et al.*, Single-cell landscape of bronchoalveolar immune cells in patients with COVID-19. *Nat. Med.* **26**, 842–844 (2020), 10.1038/s41591-020-0901-9.
4. J. J. Frere *et al.*, SARS-CoV-2 infection in hamsters and humans results in lasting and unique systemic perturbations after recovery. *Sci. Transl. Med.* **14**, eabq3059 (2022), 10.1126/scitranslmed.abq3059.
5. X. Ren *et al.*, COVID-19 immune features revealed by a large-scale single-cell transcriptome atlas. *Cell* **184**, 1895–1913 (2021), 10.1016/j.cell.2021.01.053.
6. A. C. Codo *et al.*, Elevated glucose levels favor SARS-CoV-2 infection and monocyte response through a HIF-1α/glycolysis-dependent axis. *Cell Metab.* **32**, 437–446 (2020), 10.1016/j.cmet.2020.07.007.
7. D. Butler *et al.*, Shotgun transcriptome, spatial omics, and isothermal profiling of SARS-CoV-2 infection reveals unique host responses, viral diversification, and drug interactions. *Nat. Commun.* **12**, 1660 (2021), 10.1038/s41467-021-21361-7.
8. X. Yang *et al.*, Clinical course and outcomes of critically ill patients with SARS-CoV-2 pneumonia in Wuhan, China: A single-centered, retrospective, observational study. *Lancet Respir. Med.* **8**, 475–481 (2020), 10.1016/S2213-2600(20)30079-5.
9. Q. Liu *et al.*, Pathological changes in the lungs and lymphatic organs of 12 COVID-19 autopsy cases. *Natl. Sci. Rev.* **7**, 1868–1878 (2020), 10.1093/nsr/nwaa247.
10. P. J. Busse, S. C. Christiansen, Hereditary angioedema. *N. Engl. J. Med.* **382**, 1136–1148 (2020), 10.1056/NEJMra1808012.
11. M. Mahmudpour, J. Roozbeh, M. Keshavarz, S. Farrokhi, I. Nabipour, COVID-19 cytokine storm: The anger of inflammation. *Cytokine* **133**, 155151 (2020), 10.1016/j.cyto.2020.155151.
12. A. E. Mast *et al.*, SARS-CoV-2 suppresses anticoagulant and fibrinolytic gene expression in the lung. *eLife* **10**, e64330 (2021), 10.7554/eLife.64330.
13. Z. Zhong *et al.*, New mitochondrial DNA synthesis enables NLRP3 inflammasome activation. *Nature* **560**, 198–203 (2018), 10.1038/s41586-018-0372-z.
14. M. Tigano, D. C. Vargas, S. Tremblay-Belzile, Y. Fu, A. Sfeir, Nuclear sensing of breaks in mitochondrial DNA enhances immune surveillance. *Nature* **591**, 477–481 (2021), 10.1038/s41586-021-03269-w.
15. H. Xian *et al.*, Oxidized DNA fragments exit mitochondria via mPTP- and VDAC-dependent channels to activate NLRP3 inflammasome and interferon signaling. *Immunity* **55**, 1370–1385 (2022), 10.1016/j.immuni.2022.06.007.
16. J. W. Guarnieri *et al.*, SARS-COV-2 viroporins activate the NLRP3-inflammasome by the mitochondrial permeability transition pore. *Front Immunol.* **14**, 1064293 (2023), 10.3389/fimmu.2023.1064293.
17. J. S. Riley, S. W. Tait, Mitochondrial DNA in inflammation and immunity. *EMBO Rep.* **21**, e49799 (2020), 10.15252/embr.201949799.
18. D. C. Fajgenbaum, C. H. June, Cytokine storm. *N. Engl. J. Med.* **383**, 2255–2273 (2020), 10.1056/NEJMra2026131.
19. A. Weber, P. Wasiliew, M. Kracht, Interleukin-1 (IL-1) pathway. *Sci. Signal.* **3**, cm1 (2010), 10.1126/scisignal.3105cm1.
20. R. Mezzadra *et al.*, Identification of CMTM6 and CMTM4 as PD-L1 protein regulators. *Nature* **549**, 106–110 (2017), 10.1038/nature23669.
21. D. Haslund *et al.*, Dominant-negative SERPING1 variants cause intracellular retention of C1 inhibitor in hereditary angioedema. *J. Clin. Invest.* **129**, 388–405 (2019), 10.1172/JCI98869.
22. A. Kurolap *et al.*, Establishing the role of PLVAP in protein-losing enteropathy: A homozygous missense variant leads to an attenuated phenotype. *J. Med. Genet.* **55**, 779–784 (2018), 10.1136/jmedgenet-2018-105299.
23. L. Denzer, W. Muranyi, H. Schroten, C. Schwerk, The role of PLVAP in endothelial cells. *Cell Tissue Res.* **392**, 393–412 (2023), 10.1007/s00441-023-03741-1.
24. H. Amal *et al.*, S-nitrosylation of E3 ubiquitin-protein ligase RNF213 alters non-canonical Wnt/Ca^{+2} signaling in the P301S mouse model of tauopathy. *Transl. Psychiatry* **9**, 44 (2019), 10.1038/s41398-019-0388-7.
25. R. Tashiro *et al.*, Dysregulation of Rnf 213 gene contributes to T cell response via antigen uptake, processing, and presentation. *J. Cell Physiol.* **236**, 7554–7564 (2021), 10.1002/jcp.30396.
26. J. J. Wong, Y. F. Pung, N. S. Sze, K. C. Chin, HERC5 is an IFN-induced HECT-type E3 protein ligase that mediates type I IFN-induced ISGylation of protein targets. *Proc. Natl. Acad. Sci. U.S.A.* **103**, 10735–10740 (2006), 10.1073/pnas.0600397103.
27. Y. C. Perng, D. J. Lenschow, ISG15 in antiviral immunity and beyond. *Nat. Rev. Microbiol.* **16**, 423–439 (2018), 10.1038/s41579-018-0020-5.
28. S. Jacquet, D. Pontier, L. Etienne, Rapid evolution of HERC6 and duplication of a chimeric HERC5/6 gene in rodents and bats suggest an overlooked role of HERCs in mammalian immunity. *Front Immunol.* **11**, 605270 (2020), 10.3389/fimmu.2020.605270.
29. P. Bai, Biology of poly(ADP-ribose) polymerases: The factotums of cell maintenance. *Mol. Cell* **58**, 947–958 (2015), 10.1016/j.molcel.2015.01.034.
30. S. Vavassori *et al.*, Multisystem inflammation and susceptibility to viral infections in human ZNFX1 deficiency. *J. Allergy Clin. Immunol.* **148**, 381–393 (2021), 10.1016/j.jaci.2021.03.045.
31. Y. Wang *et al.*, Mitochondria-localised ZNFX1 functions as a dsRNA sensor to initiate antiviral responses through MAVS. *Nat. Cell Biol.* **21**, 1346–1356 (2019), 10.1038/s41556-019-0416-0.
32. R. Karki *et al.*, ZBP1-dependent inflammatory cell death, PANoptosis, and cytokine storm disrupt IFN therapeutic efficacy during coronavirus infection. *Sci. Immunol.* **7**, eabo6294 (2022), 10.1126/sciimmunol.abo6294.
33. B. Szczesny *et al.*, Mitochondrial DNA damage and subsequent activation of Z-DNA binding protein 1 links oxidative stress to inflammation in epithelial cells. *Sci. Rep.* **8**, 914 (2018), 10.1038/s41598-018-19216-1.
34. J. Saada *et al.*, Oxidative stress induces Z-DNA-binding protein 1-dependent activation of microglia via mtDNA released from retinal pigment epithelial cells. *J. Biol. Chem.* **298**, 101523 (2022), 10.1016/j.jbc.2021.101523.
35. J. Nassour *et al.*, Telomere-to-mitochondria signalling by ZBP1 mediates replicative crisis. *Nature* **614**, 767–773 (2023), 10.1038/s41586-023-05710-8.
36. X. Liu, S. Xia, Z. Zhang, H. Wu, J. Lieberman, Channelling inflammation: Gasdermins in physiology and disease. *Nat. Rev. Drug. Discov.* **20**, 384–405 (2021), 10.1038/s41573-021-00154-z.
37. Y. Han *et al.*, XAF1 protects host against emerging RNA viruses by stabilizing IRF1-dependent antiviral immunity. *J. Virol.* **96**, e0077422 (2022), 10.1128/jvi.00774-22.
38. H. Xian *et al.*, Metformin inhibition of mitochondrial ATP and DNA synthesis abrogates NLRP3 inflammasome activation and pulmonary inflammation. *Immunity* **54**, 1463–1477 (2021), 10.1016/j.immuni.2021.05.004.
39. C. Huang *et al.*, Clinical features of patients infected with 2019 novel coronavirus in Wuhan, China. *Lancet* **395**, 497–506 (2020), 10.1016/s0140-6736(20)30183-5.
40. C. Dostert, M. Grusdat, E. Letellier, D. Brenner, The TNF family of ligands and receptors: Communication modules in the immune system and beyond. *Physiol. Rev.* **99**, 115–160 (2019), 10.1152/physrev.00045.2017.
41. N. I. Lore *et al.*, CXCL10 levels at hospital admission predict COVID-19 outcome: Hierarchical assessment of 53 putative inflammatory biomarkers in an observational study. *Mol. Med.* **27**, 129 (2021), 10.1186/s10020-021-00390-4.
42. V. Callahan *et al.*, The pro-inflammatory chemokines CXCL9, CXCL10 and CXCL11 are upregulated following SARS-CoV-2 infection in an AKT-dependent manner. *Viruses* **13**, 1062 (2021), 10.3390/v13061062.
43. D. Fisch *et al.*, Human GBP1 differentially targets *Salmonella* and *Toxoplasma* to license recognition of microbial ligands and caspase-mediated death. *Cell Rep.* **32**, 108008 (2020), 10.1016/j.celrep.2020.108008.
44. K. Pakos-Zebrucka *et al.*, The integrated stress response. *EMBO Rep.* **17**, 1374–1395 (2016), 10.15252/embr.201642195.
45. H. Hongo *et al.*, Comprehensive investigation of RNF213 nonsynonymous variants associated with intracranial artery stenosis. *Sci. Rep.* **10**, 11942 (2020), 10.1038/s41598-020-68888-1.
46. T. Le Voyer *et al.*, Inherited deficiency of stress granule ZNFX1 in patients with monocytosis and mycobacterial disease. *Proc. Natl. Acad. Sci. U.S.A.* **118**, e2102804118 (2021), 10.1073/pnas.2102804118.

47. Y. J. Crow, N. Manel, Aicardi-Goutières syndrome and the type I interferonopathies. *Nat. Rev. Immunol.* **15**, 429–440 (2015), 10.1038/nri3850.
48. S. Rysz *et al.*, COVID-19 pathophysiology may be driven by an imbalance in the renin-angiotensin-aldosterone system. *Nat. Commun.* **12**, 2417 (2021), 10.1038/s41467-021-22713-z.
49. N. Le Bert, S. Gasser, Advances in NKG2D ligand recognition and responses by NK cells. *Immunol. Cell Biol.* **92**, 230–236 (2014), 10.1038/icb.2013.111.
50. E. R. Stanley, V. Chitu, CSF-1 receptor signaling in myeloid cells. *Cold Spring Harb. Perspect Biol.* **6**, a021857 (2014), 10.1101/cshperspect.a021857.
51. J. Zhu, W. E. Paul, CD4 T cells: Fates, functions, and faults. *Blood* **112**, 1557–1569 (2008), 10.1182/blood-2008-05-078154.
52. H. Su, N. Na, X. Zhang, Y. Zhao, The biological function and significance of CD74 in immune diseases. *Inflamm. Res.* **66**, 209–216 (2017), 10.1007/s00011-016-0995-1.
53. L. Yang *et al.*, The signal pathways and treatment of cytokine storm in COVID-19. *Signal. Transduct. Target Ther.* **6**, 255 (2021), 10.1038/s41392-021-00679-0.
54. D. E. Place, T. D. Kanneganti, Cell death-mediated cytokine release and its therapeutic implications. *J. Exp. Med.* **216**, 1474–1486 (2019), 10.1084/jem.20181892.
55. S. Ramasamy, S. Subbian, Critical determinants of cytokine storm and type I interferon response in COVID-19 pathogenesis. *Clin. Microbiol. Rev.* **34**, e00299-20 (2021), 10.1128/CMR.00299-20.
56. D. Cosman *et al.*, Interleukin 15 and its receptor. *Ciba Found. Symp.* **195**, 221–229 (1995), 10.1002/9780470514849.ch15.
57. C. Drouet *et al.*, SERPING1 variants and C1-INH biological function: A close relationship with C1-INH-HAE. *Front. Allergy* **3**, 835503 (2022), 10.3389/falgy.2022.835503.
58. J. O. M. Almitairi *et al.*, Structure of the C1r–C1s interaction of the C1 complex of complement activation. *Proc. Natl. Acad. Sci. U.S.A.* **115**, 768–773 (2018), 10.1073/pnas.1718709115.
59. J. Sharma *et al.*, Pathophysiology of hereditary angioedema (HAE) beyond the SERPING1 gene. *Clin. Rev. Allergy Immunol.* **60**, 305–315 (2021), 10.1007/s12016-021-08835-8.
60. K. Bork *et al.*, Hereditary angioedema cosegregating with a novel kininogen 1 gene mutation changing the N-terminal cleavage site of bradykinin. *Allergy* **74**, 2479–2481 (2019), 10.1111/all.13869.
61. C. Suffritti *et al.*, High-molecular-weight kininogen cleavage correlates with disease states in the bradykinin-mediated angioedema due to hereditary C1-inhibitor deficiency. *Clin. Exp. Allergy* **44**, 1503–1514 (2014), 10.1111/cea.12293.
62. K. Bork *et al.*, Hereditary angioedema with a mutation in the plasminogen gene. *Allergy* **73**, 442–450 (2018), 10.1111/all.13270.
63. A. Recke *et al.*, Identification of the recently described plasminogen gene mutation p.Lys330Glu in a family from Northern Germany with hereditary angioedema. *Clin. Transl. Allergy* **9**, 9 (2019), 10.1186/s13601-019-0247-x.
64. K. Bork *et al.*, Novel hereditary angioedema linked with a heparan sulfate 3-O-sulfotransferase 6 gene mutation. *J. Allergy Clin. Immunol.* **148**, 1041–1048 (2021), 10.1016/j.jaci.2021.01.011.
65. S. Kattula, J. R. Byrnes, A. S. Wolberg, Fibrinogen and fibrin in hemostasis and thrombosis. *Arterioscler. Thromb. Vasc. Biol.* **37**, e13–e21 (2017), 10.1161/ATVBAHA.117.308564.
66. F. L. Macrae *et al.*, A fibrin biofilm covers blood clots and protects from microbial invasion. *J. Clin. Invest.* **128**, 3356–3368 (2018), 10.1172/JCI98734.
67. J. Jankun *et al.*, Highly stable plasminogen activator inhibitor type one (VLHL PAI-1) protects fibrin clots from tissue plasminogen activator-mediated fibrinolysis. *Int. J. Mol. Med.* **20**, 683–687 (2007).
68. W. P. Fay, A. C. Parker, L. R. Condrey, A. D. Shapiro, Human plasminogen activator inhibitor-1 (PAI-1) deficiency: Characterization of a large kindred with a null mutation in the PAI-1 gene. *Blood* **90**, 204–208 (1997).
69. M. H. Lee, E. Vosburgh, K. Anderson, J. McDonagh, Deficiency of plasma plasminogen activator inhibitor 1 results in hyperfibrinolytic bleeding. *Blood* **81**, 2357–2362 (1993).
70. J. Carvelli *et al.*, Association of COVID-19 inflammation with activation of the C5a–C5aR1 axis. *Nature* **588**, 146–150 (2020), 10.1038/s41586-020-2600-6.
71. D. J. Gorski *et al.*, Cardiac fibroblast activation and hyaluronan synthesis in response to hyperglycemia and diet-induced insulin resistance. *Sci. Rep.* **9**, 1827 (2019), 10.1038/s41598-018-36140-6.
72. S. Stridh, F. Palm, P. Hansell, Renal interstitial hyaluronan: Functional aspects during normal and pathological conditions. *Am. J. Physiol. Regul. Integr. Comp. Physiol.* **302**, R1235–1249 (2012), 10.1152/ajpregu.00332.2011.
73. Z. Bekassy, I. Lopatko Fagerstrom, M. Bader, D. Karpman, Crosstalk between the renin-angiotensin, complement and kallikrein-kinin systems in inflammation. *Nat. Rev. Immunol.* **22**, 411–428 (2022), 10.1038/s41577-021-00634-8.
74. N. Laurens, P. Koolwijk, M. P. de Maat, Fibrin structure and wound healing. *J. Thromb. Haemost.* **4**, 932–939 (2006), 10.1111/j.1538-7836.2006.01861.x.
75. D. J. Unsworth *et al.*, Studies on reticulin. I: Serological and immunohistological investigations of the occurrence of collagen type III, fibronectin and the non-collagenous glycoprotein of Pras and Glynn in reticulin. *Br. J. Exp. Pathol.* **63**, 154–166 (1982).
76. A. A. Zahr *et al.*, Bone marrow fibrosis in myelofibrosis: Pathogenesis, prognosis and targeted strategies. *Haematologica* **101**, 660–671 (2016), 10.3324/haematol.2015.141283.
77. D. J. Kuter, B. Bain, G. Mufti, A. Bagg, R. P. Hasserjian, Bone marrow fibrosis: Pathophysiology and clinical significance of increased bone marrow stromal fibres. *Br. J. Haematol.* **139**, 351–362 (2007), 10.1111/j.1365-2141.2007.06807.x.
78. C. Kityo *et al.*, Lymphoid tissue fibrosis is associated with impaired vaccine responses. *J. Clin. Invest.* **128**, 2763–2773 (2018), 10.1172/JCI97377.
79. T. W. Schacker *et al.*, Lymphatic tissue fibrosis is associated with reduced numbers of naive CD4+ T cells in human immunodeficiency virus type 1 infection. *Clin. Vacc. Immunol.* **13**, 556–560 (2006), 10.1128/CVI.13.5.556-560.2006.
80. J. W. Guarnieri *et al.*, Core mitochondrial genes are down-regulated during SARS-CoV-2 infection of rodent and human hosts. *Sci. Transl. Med.* **15**, eabq1533 (2023), 10.1126/scitranslmed.abq1533.
81. J. W. Guarnieri *et al.*, SARS-CoV-2 mitochondrial metabolic and epigenomic reprogramming in COVID-19. *Pharmacol. Res.* **204**, 107170 (2024), 10.1016/j.phrs.2024.107170.
82. J. W. Guarnieri *et al.*, Mitochondrial antioxidants abate SARS-COV-2 pathology in mice. *Proc. Natl. Acad. Sci. U.S.A.* **121**, e2321972121 (2024), 10.1073/pnas.2321972121.
83. J. J. VanPortfliet, C. Chute, Y. Lei, T. E. Shutt, A. P. West, Mitochondrial DNA release and sensing in innate immune responses. *Hum. Mol. Genet.* **33**, R80–R91 (2024), 10.1093/hmg/ddae031.
84. Y. Lei *et al.*, Cooperative sensing of mitochondrial DNA by ZBP1 and cGAS promotes cardiotoxicity. *Cell* **186**, 3013–3032 (2023), 10.1016/j.cell.2023.05.039.
85. J. Haltom *et al.*, SARS-CoV-2 orphan gene ORF10 contributes to more severe COVID-19 disease. medRxiv [Preprint] (2023). https://doi.org/10.1101/2023.11.27.23298847 (Accessed 12 January 2023).
86. X. Guo *et al.*, Mitochondrial stress is relayed to the cytosol by an OMA1-DELE1-HRI pathway. *Nature* **579**, 427–432 (2020), 10.1038/s41586-020-2078-2.
87. M. Costa-Mattioli, P. Walter, The integrated stress response: From mechanism to disease. *Science* **368**, eaat5314 (2020), 10.1126/science.aat5314.
88. C. Hetz, The unfolded protein response: Controlling cell fate decisions under ER stress and beyond. *Nat. Rev. Mol. Cell Biol.* **13**, 89–102 (2012), 10.1038/nrm3270.
89. T. Shpilka, C. M. Haynes, The mitochondrial UPR: Mechanisms, physiological functions and implications in ageing. *Nat. Rev. Mol. Cell Biol.* **19**, 109–120 (2018), 10.1038/nrm.2017.110.
90. R. H. Houtkooper *et al.*, Mitonuclear protein imbalance as a conserved longevity mechanism. *Nature* **497**, 451–457 (2013), 10.1038/nature12188.
91. V. S. LeBleu *et al.*, PGC-1alpha mediates mitochondrial biogenesis and oxidative phosphorylation in cancer cells to promote metastasis. *Nat. Cell Biol.* **16**, 992–1003 (2014), 10.1038/ncb3039.
92. D. Tang, X. Chen, R. Kang, G. Kroemer, Ferroptosis: Molecular mechanisms and health implications. *Cell Res.* **31**, 107–125 (2021), 10.1038/s41422-020-00441-1.
93. S. Deshwal *et al.*, Mitochondria regulate intracellular coenzyme Q transport and ferroptotic resistance via STARD7. *Nat. Cell Biol.* **25**, 246–257 (2023), 10.1038/s41556-022-01071-y.
94. J. T. McDonald *et al.*, Role of miR-2392 in driving SARS-CoV-2 infection. *Cell Rep.* **37**, 109839 (2021), 10.1016/j.celrep.2021.109839.
95. S. L. Lage *et al.*, Persistent oxidative stress and inflammasome activation in CD14. *Front. Immunol.* **12**, 799558 (2021), 10.3389/fimmu.2021.799558.
96. A. C. Ferreira *et al.*, SARS-CoV-2 engages inflammasome and pyroptosis in human primary monocytes. *Cell Death Discov.* **7**, 43 (2021), 10.1038/s41420-021-00428-w.
97. T. S. Rodrigues *et al.*, Inflammasomes are activated in response to SARS-CoV-2 infection and are associated with COVID-19 severity in patients. *J. Exp. Med.* **218**, e20201707 (2021), 10.1084/jem.20201707.
98. R. L. Furler *et al.*, Histoarchitectural deterioration of lymphoid tissues in HIV-1 infection and in aging. *AIDS Res. Hum. Retroviruses* **35**, 1148–1159 (2019), 10.1089/AID.2019.0156.
99. F. N. Morgado, A. V. A. da Silva, R. Porrozzi, Infectious diseases and the lymphoid extracellular matrix remodeling: A focus on conduit system. *Cells* **9**, 725 (2020), 10.3390/cells9030725.
100. E. A. Sayed *et al.*, Induction of liver fibrosis by CCl_4 mediates pathological alterations in the spleen and lymph nodes: The potential therapeutic role of propolis. *Saudi J. Biol. Sci.* **28**, 1272–1282 (2021), 10.1016/j.sjbs.2020.11.068.
101. X. Li *et al.*, Lymph node fibroblastic reticular cells deposit fibrosis-associated collagen following organ transplantation. *J. Clin. Invest.* **130**, 4182–4194 (2020), 10.1172/JCI136618.
102. B. Henry *et al.*, Lymphopenia and neutrophilia at admission predicts severity and mortality in patients with COVID-19: A meta-analysis. *Acta Biomed.* **91**, e2020008 (2020), 10.23750/abm.v91i3.10217.
103. R. Alon *et al.*, Leukocyte trafficking to the lungs and beyond: Lessons from influenza for COVID-19. *Nat. Rev. Immunol.* **21**, 49–64 (2021), 10.1038/s41577-020-00470-2.
104. B. Diao *et al.*, Reduction and functional exhaustion of T cells in patients with coronavirus disease 2019 (COVID-19). *Front. Immunol.* **11**, 827 (2020), 10.3389/fimmu.2020.00827.
105. N. Kaneko *et al.*, Loss of Bcl-6-expressing T follicular helper cells and germinal centers in COVID-19. *Cell* **183**, 143–157 (2020), 10.1016/j.cell.2020.08.025.
106. Y. Q. Duan *et al.*, Deficiency of Tfh cells and germinal center in deceased COVID-19 patients. *Curr. Med. Sci.* **40**, 618–624 (2020), 10.1007/s11596-020-2225-x.
107. J. D. Haslbauer *et al.*, Vascular damage, thromboinflammation, plasmablast activation, T-cell dysregulation and pathological histiocytic response in pulmonary draining lymph nodes of COVID-19. *Front. Immunol.* **12**, 763098 (2021), 10.3389/fimmu.2021.763098.
108. Q. Xiang *et al.*, SARS-CoV-2 induces lymphocytopenia by promoting inflammation and decimates secondary lymphoid organs. *Front. Immunol.* **12**, 661052 (2021), 10.3389/fimmu.2021.661052.
109. A. Abdullaev *et al.*, Viral load and patterns of SARS-CoV-2 dissemination to the lungs, mediastinal lymph nodes, and spleen of patients with COVID-19 associated lymphopenia. *Viruses* **13**, 1410 (2021), 10.3390/v13071410.
110. B. J. Laidlaw, A. H. Ellebedy, The germinal centre B cell response to SARS-CoV-2. *Nat. Rev. Immunol.* **22**, 7–18 (2022), 10.1038/s41577-021-00657-1.
111. C. Phetsouphanh *et al.*, Immunological dysfunction persists for 8 months following initial mild-to-moderate SARS-CoV-2 infection. *Nat Immunol* **23**, 210–216 (2022), 10.1038/s41590-021-01113-x.
112. J. Park *et al.*, System-wide transcriptome damage and tissue identity loss in COVID-19 patients. *Cell Rep. Med.* **3**, 100522 (2022), 10.1016/j.xcrm.2022.100522.
113. S. R. Leist *et al.*, A mouse-adapted SARS-CoV-2 induces acute lung injury and mortality in standard laboratory mice. *Cell* **183**, 1070–1085 (2020), 10.1016/j.cell.2020.09.050.
114. H. K. Lee *et al.*, Immune transcriptome analysis of COVID-19 patients infected with SARS-CoV-2 variants carrying the E484K escape mutation identifies a distinct gene module. *Sci. Rep.* **12**, 2784 (2022), 10.1038/s41598-022-06752-0.
115. H. K. Lee *et al.*, Prior vaccination exceeds prior infection in eliciting innate and humoral immune responses in Omicron infected outpatients. *Front. Immunol.* **13**, 916686 (2022), 10.3389/fimmu.2022.916686.
116. S. A. Richard *et al.*, COVID-19 outcomes among US military health system beneficiaries include complications across multiple organ systems and substantial functional impairment. *Open Forum. Infect. Dis.* **8**, ofab556 (2021), 10.1093/ofid/ofab556.
117. C. Mason, Shotgun Transcriptome and Isothermal Profiling of SARS-CoV-2 Infection Reveals Unique Host Responses, Viral Diversification, and Drug Interactions. NCBI. https://www.ncbi.nlm.nih.gov/projects/gap/cgi-bin/study.cgi?study_id=phs002258.v1.p1. Deposited 15 January 2021.
118. J. C. Schisler, W. Sanders, V. K. Baxter, M. T. Heise, Targeted down regulation of core mitochondrial genes during SARS-CoV-2 infection. Gene Expression Omnibus. https://www.ncbi.nlm.nih.gov/geo/query/acc.cgi?acc=GSE221510. Deposited 21 December 2022.
119. J. J. Frere, B. R. Tenoever, Transcriptional Profiling of SARS-CoV-2 and IAV across Syrian golden hamster brain regions and peripheral tissues at early and late time points post-infection. Gene Expression Omnibus. https://www.ncbi.nlm.nih.gov/geo/query/acc.cgi?acc=GSE203001. Deposited 13 May 2022.
120. A. Beheshti, P. Grabham, 3D Human Umbilical Vein Endothelial Cells (HUVECs) irradiated with GCR simulated irradiation with miRNA based countermeasures. NASA Open Science Data Repository's (OSDR) Biological Data Management Environment. https://osdr.nasa.gov/bio/repo. Deposited 12 December 2022.